nature communications

Article

https://doi.org/10.1038/s41467-025-60308-0

Reduction of neuronal activity mediated by blood-vessel regression in the adult brain

Received: 21 August 2021

Accepted: 16 May 2025

Published online: 01 July 2025

Check for updates

Xiaofei Gao[1,44], Xing-jun Chen[2,3,4,44], Meng Ye[2,3,5,6], Jun-Liszt Li[2,4], Nannan Lu[1,7], Di Yao[2,5], Bo Ci[1], Fei Chen[1,8], Lijun Zheng[2,5], Yating Yi[9], Shiwen Zhang[9], Zhanying Bi[2,10], Xinwei Gao[2], Yuanlei Yue[11], Tingbo Li[12], Jiafu Lin[13], Ying-Chao Shi[14], Kaibin Shi[15], Nicholas E. Propson[16], Yubin Huang[17], Katherine Poinsatte[18], Zhaohuan Zhang[1,19], Dale B. Bosco[20], Shi-bing Yang[21,22], Ralf H. Adams[23], Volkhard Lindner[24], Fen Huang[21,43], Long-Jun Wu[20], Hui Zheng[16], Simon Hippenmeyer[25,26], Ann M. Stowe[18,27], Bo Peng[28], Marta Margeta[29], Qingchun Guo[2,30], Xiaoqun Wang[6,31,32], Qiang Liu[33], Jakob Körbelin[34], Martin Trepel[35], Hui Lu[36], Guoen Cai[13], Bo O. Zhou[37], Bo Shen[38,39], Ying-mei Lu[40], Wenzhi Sun[2,5], Jie-Min Jia[12], Feng Han[41], Hu Zhao[2,3], Robert M. Bachoo[18,42] & Woo-ping Ge[2,3,6] ✉

The brain vasculature supplies neurons with glucose and oxygen, but little is known about how vascular plasticity contributes to brain function. Using longitudinal in vivo imaging, we report that a substantial proportion of blood vessels in the adult mouse brain sporadically occlude and regress. Their regression proceeds through sequential stages of blood-flow occlusion, endothelial cell collapse, relocation or loss of pericytes, and retraction of glial endfeet. Regressing vessels are found to be widespread in mouse, monkey and human brains. We further reveal that blood vessel regression cause a reduction of neuronal activity due to a dysfunction in mitochondrial metabolism and glutamate production. Our results elucidate the mechanism of vessel regression and its role in neuronal function in the adult brain.

Microvessels are composed of two closely interacting cell types, namely endothelial cells and pericytes[1], that are embedded within the endfeet of astrocytes[2]. Neurons, astrocytic endfeet, pericytes, and endothelial cells as well as the vascular basal laminar layers form the neurovascular unit that coordinates neuronal function[3–6]. Dysfunction or dysregulation of the neurovascular unit is associated with many diseases including stroke and Alzheimer's disease[7].

The density of brain vasculature and neurons declines significantly during normal aging (10–30%), and this decrease reaches 40–60% for Alzheimer's patients[8–10]. However, little is known about how blood-vessel dynamics change with age and how this affects the activity of the adult mammalian brain[11–13]. Vessel regression was reported nearly two centuries ago[10] and has been studied in the vasculature of embryonic and postnatal rodents[14–17] and zebrafish[18,19]. Several molecules (e.g., Wnt, Angiopoietin, Nrarp, VEGF, etc.) are found to be involved in normal vessel regression in developing organs[20–24]. However, the mechanisms underlying vessel regression are largely unknown, as are the fates of the various cellular components of the neurovascular unit. In this work, using genetic methods to specifically label endothelial cells, pericytes, and glial cells with different fluorescent proteins, we performed longitudinal in vivo imaging of functional microcirculation for up to 6 months, enabling a comprehensive understanding of vessel regression as the brain develops and ages and how vessel regression-related changes in the microcirculation contribute to neuronal activity in the adult brain.

Results

Alteration of the microcirculation in the adult mouse brain

To evaluate the plasticity of the blood vasculature in the adult brain, we measured functional blood flow after administering FITC-dextran

A full list of affiliations appears at the end of the paper. ✉e-mail: woopingge@cibr.ac.cn

(500 kDa) to normal mice via the tail vein (Fig. 1a). Blood flow rate was assessed by counting blood cells passing through the vessel. With this strategy, we monitored blood circulation within the same region of the cerebral cortex weekly for 3–6 months (Fig. 1b). Surprisingly, we found that 1.7% of the microvessels became non-functional (i.e., no FITC signal) across the entire field within a 5-week window (Fig. 1c). Interestingly, blood flow to ~75% of the occluded microvessels, which were observed at day 1, was restored within a week (76.2%, $n = 16$ of 21, from 8 mice). In the remaining vessels (i.e., occluded vessels), reperfusion was undetectable for >2 months after occlusion was first initiated, likely reflecting permanent functional loss (Fig. 1b, d, e). Due to the small diameter of the string structure (0.5–1μm) and the difficulty in visualizing a large portion of the string structure under in vivo imaging, we were only able to successfully trace 2–4 regressive vessels in a mouse across all time points over 3 to 6 months. It is important to note that these vessels were not from the same region, as only approximately 0.34% of vessels enter the regression process within a week. These results demonstrated that a substantial number of blood vessels in the brain undergo temporary or permanent cessation of blood flow under physiological conditions.

To determine whether loss of reperfusion in the microcirculation led to vessel regression, we used transgenic mouse strain *NG2DsRedBAC*[25] for live imaging of pericytes via labeling with the fluorescent protein DsRed (Fig. 1d, Supplementary Video 1), which is specific for pericytes in veins, capillaries, and smooth-muscle cells in arteries/arterioles in adult mouse brains[26,27](also see Supplementary Fig. 1). We detected that occlusion of blood flow for >1 week resulted in the disappearance of blood vessels (100%, $n = 8$ of 8 regressing vessels from 3 mice, Fig. 1d, Supplementary Videos 2–4). Based on our staining results for different vascular cell types (Figs. 2–4), loss of pericytes indicated near-complete vessel regression in all cases.

Distribution and properties of regressing vessels in the adult brain of different mammals

Endothelial cells and pericytes are completely enwrapped by a sheath comprising the extracellular matrix molecules laminin and collagen IV[1]. Antibodies specific for collagen IV and laminin have been used to stain regressive vessels in the brains of different species[28,29], but the distribution of regressing vessels throughout the mammalian brain has never been determined. Labeling blood vessels with anti-laminin or anti-collagen IV revealed three distinct regressive vessel types in mouse, monkey, and human brains (Fig. 2). The first type (Type I, T1) constituted 70–80% of all regressive vessels and appeared as a thin, string-like process (1–2 μm) connecting two neighboring blood vessels, no soma was associated with this type (Fig. 2a, c). The second type (Type II, T2) included a single soma situated at one end of the process, adjacent to neighboring blood vessels (Fig. 2a, c). The third type (Type III, T3) had a single soma located in the middle of the laminin-positive process with both ends of its processes connecting neighboring blood vessels (Fig. 2a, c). The abundance of these three types of regressing vessels was similar in human and mouse brain sections (Fig. 2j) (Types I, II, III in humans were 69.0%, 23.5%, and 7.5%, respectively, $n = 652$; in mouse, 80.0%, 17.6%, and 2.4%, $n = 1019$ regressive vessels from 7 mice; Fig. 2j). We further performed additional brain tissue staining using samples from three more human subjects of different ages (22, 37, and 38 years old, see Supplementary Fig. 2–4), and we observed similar phenomena, suggesting that the observed phenomenon may be generalized in the adult human brain.

To understand how the distribution of regressive vessels in the rodent brain varies with age, mouse whole-brain sections were scanned at high resolution (Supplementary Fig. 5), and tiled images were analyzed for each brain section (Fig. 2d–f, Supplementary Video 5). The same strategy was used to detect regressing vessels in several human brain regions including the hippocampus, cerebellum, and cerebral cortex (Fig. 2g–i). The regressing vessels were widely distributed in nearly all major brain regions in mice (Fig. 2d–f, Supplementary Video 5), and the length of regressive vessels did not differ between juvenile and adult mouse brains (P17, 22.95 ± 0.82 μm, $n = 227$ regressing vessels, $n = 4$ mice; P340, 21.72 ± 1.18 μm, $n = 138$ regressing vessels, $n = 4$ mice). Interestingly, there was a significant decrease in the density of regressing vessels in the aging brains, but the regressive vessels were still abundant in aged brains (P100, 262.3 ± 11.1/mm^3, $n = 4$ mice; P800–820, 177.9 ± 12.6/mm^3, $n = 4$ mice; Fig. 2k). On average, the regressing vessels were significantly longer in the adult human brain than in mouse brain ($n = 1$, male subject, 39.4 ± 2.2 μm, $n = 132$ regressing vessels; mouse, 22.4 ± 0.9 μm, $n = 365$ regressing vessels, Fig. 2l, m). Interestingly, the hippocampus had the highest density of regressing vessels among all the brain regions we assessed (hippocampus, $n = 7$ mice; cerebral cortex, $n = 7$ mice; thalamus, $n = 6$ mice; hypothalamus, $n = 6$ mice; Fig. 2n).

Mechanism of blood-vessel regression in the brain

Although blood-vessel regression has been studied for decades[29], the underlying cellular mechanism remains controversial, including the fate of pericytes. Pericytes enwrap endothelial cells[1], but it is unclear whether regressive vessels form with laminin alone, also known as ghost structures or string vessels labeled by anti-collagen IV or anti-laminin[29,30], or whether they include endothelial cells and/or pericytes. An analysis of the staining (anti-CD31 and anti-laminin/anti-collagen IV) of the cellular constituents of ~200 regressive vessels in brain sections from *NG2DsRedBAC* mice revealed the presence of pericytes in ~90% of remnants of regressive vessels (Fig. 3a–c). Similar results were obtained with brain sections of *Pdgfrb-Cre::Ai14* (Supplementary Fig. 6), which is a mouse strain for labeling pericytes and smooth muscle cells in the brain[31] (also see Supplementary Fig. 7). Capillaries are composed of laminin layers, endothelial cells, and pericytes[1], implying seven distinct possible combinations of cell components for any given regressive vessel. Only three of these combinations were found in the regressive structures that we analyzed (Fig. 3c): a very small percentage of regressive vessels were laminin$^+$ DsRed$^+$CD31$^+$ (7.3%, 13 of 179, i.e., pericytes, laminin layer and endothelial cells) or laminin$^+$ only (10.1%, 18 of 179, i.e., laminin layer only), and the remainder contained laminin layers and pericytes but no endothelial cells (laminin$^+$DsRed$^+$CD31$^-$, 82.7%, 148 of 179). These results indicated that endothelial cells are eliminated prior to the loss of pericytes during vessel regression. This differs from previous reports that concluded that string-like vessels (i.e., regressing vessel) are “ghost” vessels comprised only of laminin matrix[29]. Our results indicate that ~90% of regressing vessel structures contained laminin- or collagen-positive layers and pericytes (Fig. 3c). These findings were supported by anti-collagen IV staining of brain sections of *Cdh5-CreER::Ai14* mice (Supplementary Figs. 8 and 9), which is a specific mouse strain for labeling endothelial cells with tdTomato in the brain. We detected very few regressive vessels that contained an endothelial cell component (7.6%, $n = 28$ of 369 regressive vessels). This was verified by in vivo imaging results from *Cdh5-CreER::Ai6::NG2DsRedBAC* mice, in which the endothelial cells[32] and pericytes were labeled with ZsGreen and DsRed, respectively (Supplementary Fig. 9). These results indicate the endothelial cells initially retracted in regressing vessels, after which pericytes were retained beyond the 3-week time point (Supplementary Fig. 9).

To investigate pericyte fate during vessel regression in the adult brain. We imaged pericytes in regressing vessels from cortical regions of *NG2DsRedBAC* mice. Blood flow was monitored with FITC-dextran or with blood cells labeled with 3,3′-dioctadecyloxacarbocyanine perchlorate (commonly called DiO). The morphology of pericytes in regressing vessels varied, as assessed in vivo (Fig. 3d, e), which represented different stages of vessel regression observed in fixed tissues (Fig. 2a–c). Longitudinal live imaging revealed that the half-life of regressing vessels was ~5 weeks ($n = 58$ from 6 mice, Fig. 3f–i).

https://doi.org/10.1038/s41467-025-60308-0

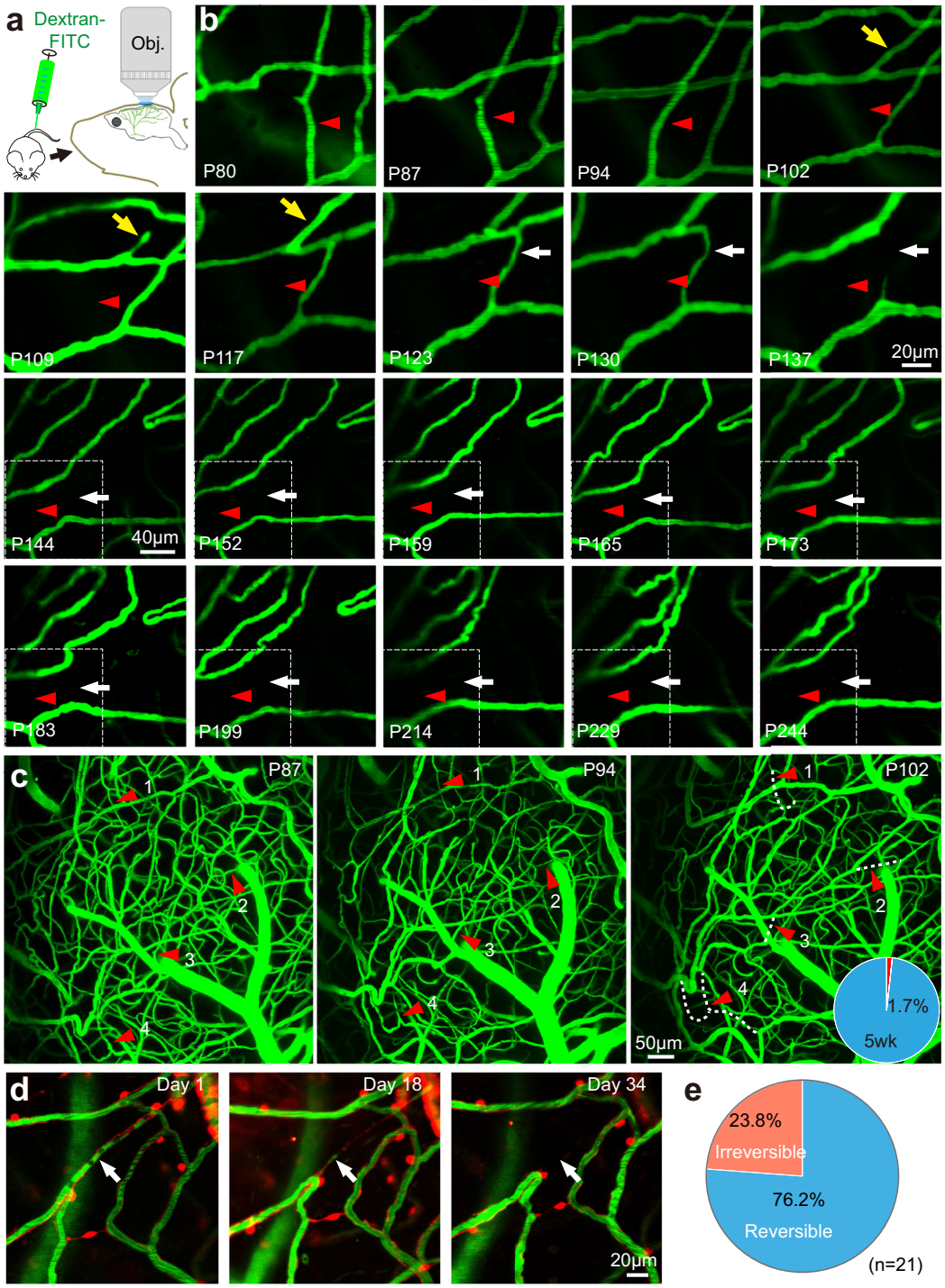

Fig. 1 | Alteration of the microcirculation in the adult mouse brain. a Schematic showing injection of dextran-FITC into the bloodstream via the tail vein and live imaging of functional brain microcirculation through a cranial window. **b** Time-lapse imaging of the microcirculation of a cortical region in a mouse from its postnatal day (P)80 to P244. The same region was imaged once every week for 6 months. Two different vessels (white arrows and red arrowheads) became occluded, and blood flow was not restored after 102 and 137 days (i.e., which were 142 and 107 days after occlusion, respectively). Blood flow in one occluded blood vessel was restored (yellow arrows). From day 144, each image has a larger field than prior images. **c** One example of images of all occluded vessels in the field imaged. The lengths of these occluded vessels (white dashed lines, 1 to 4) were used to normalize all vessels in the field. The percentages of occluded blood vessels, which were normalized to all blood vessels in terms of length, are shown in the pie chart in the right panel. 5 wks, time-lapse imaging of the region shown in **c** over 5 weeks. **d** Blood-flow occlusion precedes vessel regression. DsRed, pericytes in the brain of *NG2DsRedBAC* transgenic mice; green, FITC-dextran signal in blood vessels. Arrows indicate a regressing blood vessel. **e** Summary of results for blood vessels with or without blood-flow restoration (i.e., reperfusion) within a week after detecting occlusion. $n = 21$: number of occluded blood vessels imaged.

https://doi.org/10.1038/s41467-025-60308-0

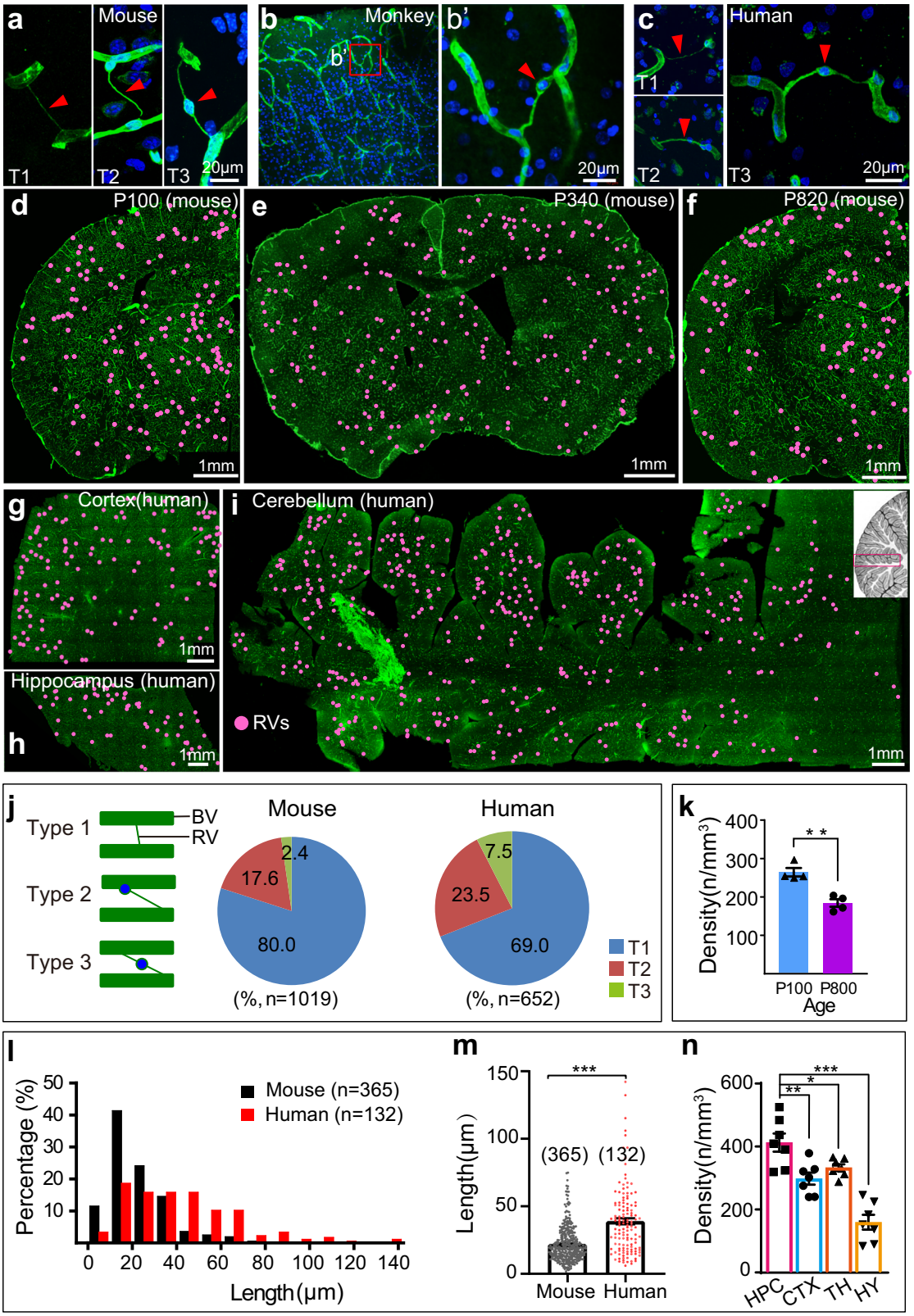

Pericytes from regressing vessels had three distinguishable fates: ~30% disappeared, likely by apoptosis (Fig. 3f); 20% remained stable, with no obvious change in morphology or somatic location over the 8-weeks period (Fig. 3g); the remaining ~50% retracted one of their processes, and the soma relocated to a neighboring blood vessel (Fig. 3h). These results indicated that, in comparison with endothelial cells, pericytes in regressing vessels maintained a relatively stable structure. To further verify these results, we took advantage of a mosaic analysis with double markers (*MADM*) transgenic mouse line[33] for labeling single pericytes through breeding them with *Hprt-Cre* mice in which the Cre cassette is inserted into the X-linked gene *Hprt*. These mice have Cre recombinase in their oocytes, which excises a floxed sequence at the zygote or early cleavage stage[34]. In *Hprt-Cre::MADM-7GT* mice[35], brain cells, including pericytes, were sparsely labeled with GFP and/or DsRed

Fig. 2 | Distribution and properties of regressing vessels in the adult brain of different mammals. a Three typical types of regressive vessel structures in the adult mouse brain (T1, T2, T3). Blue, nuclei stained with Hoechst 33342; green, anti-laminin; arrowheads, regressing vessels. **b** Regressing vessels detected in the cortical section of a 3-year-old monkey. **c** Three types of representative regressing vessels from human brain tissues. **d**–**f** Distribution of all regressing vessels in whole-brain/hemisphere sections of mice at P100, P340, and P820. Each dot represents one regressive vessel. All vessels were labeled with anti-laminin or anti-collagen IV. Distribution of regressive vessels detected in three different brain regions of a 45-year-old human male: cerebral cortex (**g**), hippocampus (**h**), cerebellum (**i**). The location of the imaged section from the cerebellum is shown in the top right corner in **i** outlined in red. All vessels were labeled with anti-laminin. Slice thickness, 70 μm. **j** Schematic diagrams and percentages of three different types of regressive structures found in human and mouse brains (regressive vessels, $n = 1019$ from 7 mice; $n = 652$ from 1 male subject). Green, blood vessels; blue, soma. **k** Density of regressive vessels in the brain of a young adult (~P100, $n = 4$ mice) and old mouse (~P800, $n = 4$ mice). **l** Length distribution of regressing vessels from human and mouse brains. The x axis represents the length of regressing vessels. **m** Average length of regressing vessels in human ($n = 132$ regressive vessels from 1 male) and mouse brains ($n = 365$ regressive vessels from 7 mice). **n** Comparison of the density of regressing vessels from different mouse brain regions ($n = 7$ areas). HPC hippocampus, CTX cerebral cortex, TH thalamus, HY hypothalamus. $^{*}p < 0.05$; $^{**}p < 0.01$, $^{***}p < 0.001$, two-tailed unpaired t-test. All error bars indicate SEM.

(Fig. 4), allowing high-resolution imaging of individual pericytes of regressing vessels (Fig. 4). Surprisingly, these single pericytes in regressing blood vessels had two mature and complex processes that wrapped around adjacent blood vessels (100%, $n = 8$ of 8, Fig. 4), both complex processes are connected with a string structure from the same single pericyte, rather than two pericytes, which is consistent with our results from long-term in vivo imaging in *NG2DsRedBAC* mice (Fig. 3), but different from interpericyte tunneling nanotubes reported in a recent study[36]. These results indicated that remnant pericytes of regressing vessels were relatively stable constituents of regressing vessels, which is consistent with our in vivo time-lapse imaging of vessel regression (Fig. 3f). We observed that approximately 20% of regressing vessels exhibited this prolonged duration. However, evaluating the function of these vessels poses a challenge, as it is difficult to predict which vessels will remain stable and which will regress over time. These "putative RVs" may possess special functions in the brain, as suggested by previous research articles[36](e.g., IP-TNT).

Astrocytes are the most prevalent glial cells in the mammalian brain. They extend two types of processes from their cell bodies: fine perisynaptic processes that cover most neuronal synapses, and larger processes, known as endfeet, that primarily extend to and make tight contacts with blood vessels, thus covering >99% of the abluminal vascular surface in the adult brain[2]. Astrocytic endfeet ferry glucose from blood to neurons and are vital for neuronal function[4,37]. Despite being one of the critical cells of the neurovascular unit, the fate of astrocytic endfeet in vessel regression is unclear. Therefore, we stained brain sections of *hGFAP-GFP*[38] or *Aldh1L1-EGFP*[39] transgenic mice with anti-laminin or anti-collagen IV to locate regressing vessels, all of which were fully enwrapped by astrocytic endfeet (100%, $n = 34$ of 34, Fig. 3j, k). These results indicated that vessel regression was not initiated by the retraction of astrocytic endfeet. Overall, our results demonstrate that vessel regression in mammals is mediated by distinct steps: blood flow is occluded, endothelial cells are reabsorbed, and pericytes relocate or die; finally, glial endfeet lose contact with vessels (Fig. 3l). We further used the methods to evaluate BBB integrity reported in previous studies. We stained brain sections with IgM, a method for detecting BBB leakage, and found no leakage from any of the three types of regressing vessels ($n = 0$ of 20 regressive vessels, as shown in Supplementary Fig. 10).

Exaggerated blood vessel regression leads to a reduction of neuronal activity

In the mammalian brain, blood-vessel density decreases substantially with age[8,29]. Interestingly, we hardly detected newly formed functional blood vessels in the adult brain, even when we imaged the same regions for months (Fig. 1). Thus, continued vessel regression increases the distance between neurons and blood vessels. Because few vessels actually undergo regression in a short time window (i.e., ~0.34% per week), it was difficult to predict which vessels might regress for the purpose of imaging neuronal activity in the same region for months. To assess how vessel regression affects brain function, we created a conditional knockout of *Tak1* in endothelial cells[40], as Tak1 is reported to be involved in vessel regression[40]. *Tak1* knockout increased vessel regression by 6–8 fold at 1–3 weeks after administration of tamoxifen to *Cdh5-CreER::Tak1*$^{fl/fl}$ mice (*Tak1*$^{fl/fl}$, $n = 5$ mice; *Tak1 CKO*, $n = 6$ mice, Fig. 5a, b). This allowed us to possibly evaluate the effect of vessel regression on neuronal activity in a relative shorter time frame. To image neuronal activity, we transfected neurons with adeno-associated virus (AAV) vectors expressing GCaMP (*AAV-CAMKII-GCaMP6m*) in cortical layers 2–4 (Fig. 5c–f) at one month before tamoxifen injection. Neuronal activity was measured before and after conditional knockout of *Tak1* in endothelial cells in conscious mice (Fig. 5c–k). To ensure detection of subtle differences in activity before and after vessel regression, we imaged and compared the same neurons at different time points. We observed that neuronal activity declined significantly 1–2 weeks after the conditional knockout of *Tak1* (2.83 ± 0.26 spikes/min before tamoxifen administration vs. 1.43 ± 0.19 spikes/min after administration ($n = 65$ neurons from 5 mice; Fig. 5e, g, i, j, Supplementary Video 6–9). The frequency of all spikes decreased in the *Tak1*-knockout group, indicating that exaggerated vessel regression reduced neuronal activity. In control mice, however, neuronal activity was not affected by tamoxifen (or by the carrier solution, as a control; 2.60 ± 0.24 spikes/min vs. 2.76 ± 0.23 spikes/min, respectively; $n = 45$ neurons from 5 mice; Fig. 5f, h, k, and l, Supplementary Video 6–9). To detect whether potential vessel leakage occurred in the brain of *Cdh5-CreER::Tak1*$^{fl/fl}$ mice, we stained brain sections with fibrinogen within 1–2 weeks after tamoxifen administration. Our analysis revealed no detectable fibrinogen signal in the neighboring regions near the regressive vessels, suggesting minimal leakage from the regressing vessels (Supplementary Fig. 11). These results indicated that exaggerated vessel regression in the microcirculation could causally mediate the reduction of neuronal activity. We cannot exclude the possibility that there is a physiological reorganization of microvessels redistributing blood flow more optimally. Indeed, we observed that the regression of one blood vessel can alter the blood flow speed and direction of neighboring micro-vessels. However, the challenge lies in definitively proving whether this alteration ultimately "optimizes" blood flow and does not alter neuronal activity.

To mitigate the influence of peripheral organs, we used *AAV-BR1-Cre* to induce *Tak1* deletion specifically in brain vasculature and subsequently assessed neuronal calcium activity. *AAV-BR1* has been previously reported for its specificity in targeting vasculature within the central nervous system, including the brain[41]. By utilizing this approach, we aimed to eliminate the possibility of secondary effects from peripheral organs in *Cdh5-CreER::Tak1*$^{fl/fl}$ mice. Prior to administering *AAV-BR1-Cre* to these mice, we infected neurons with *AAV/DJ8-CAMKII-GCaMP6m*, allowing us to measure neuronal calcium activity before and after blood vessels were infected with *AAV-BR1-Cre*. In this experiment, we analyzed calcium activity from 151 neurons ($n = 4$ mice) in the cerebral cortex of these mice. The observed phenomena were consistent with those detected in *Cdh5-CreER::Tak1*$^{fl/fl}$ mice, enhancing the credibility of our assessment of the effect of vessel regression on neuronal activity (Supplementary Fig. 12).

https://doi.org/10.1038/s41467-025-60308-0

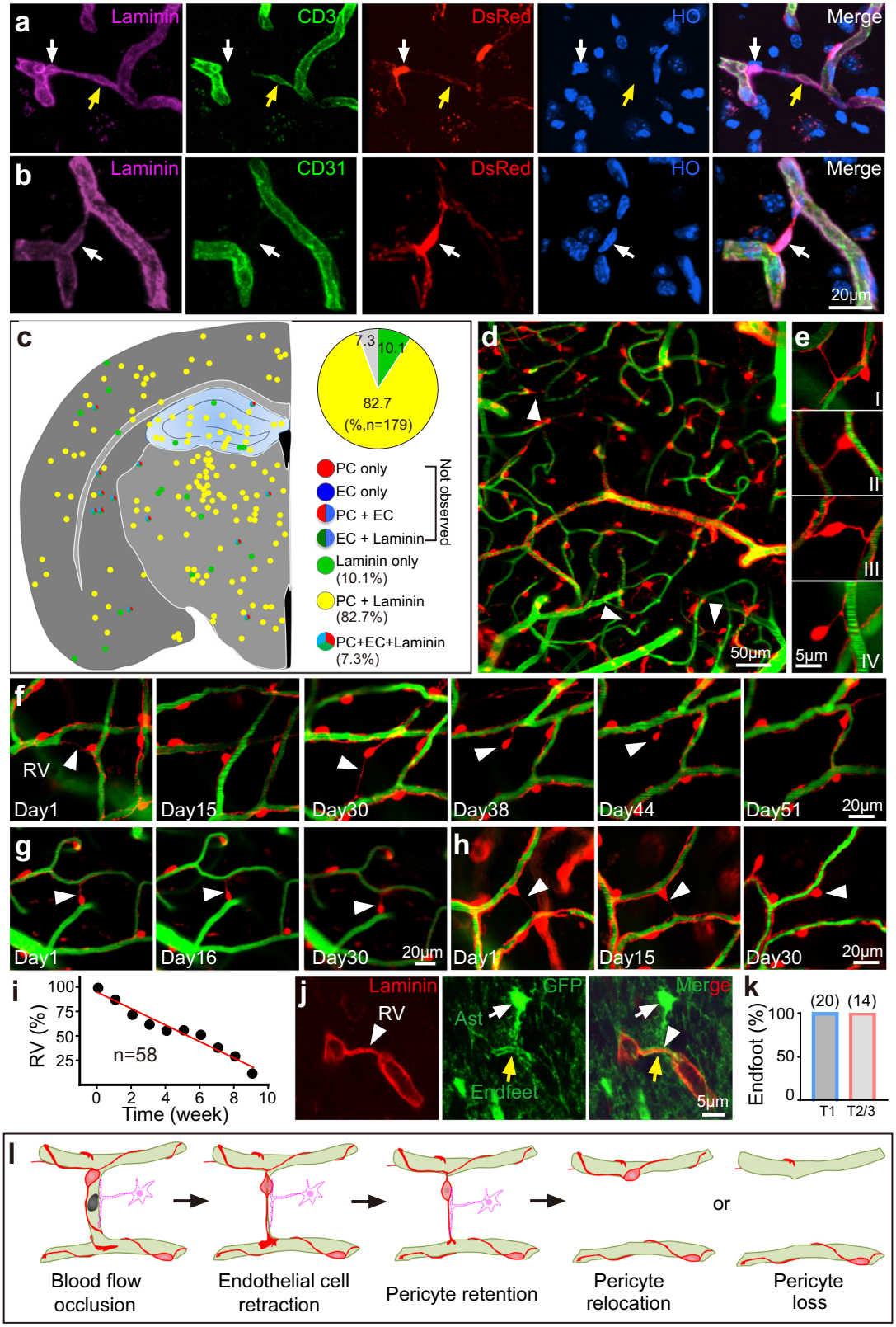

After injecting *AAV-BR1-Cre* viruses into *Ai14* reporter mice, we labeled lymphatic vessels using antibodies against Lyve-1. Our findings revealed rare infection of cells from the lymphatic system by *AAV-BR1-Cre* (Supplementary Fig. 13). Therefore, these results effectively eliminate the possibility of effects from blood vessels in peripheral organs or endothelial cells from the lymphatic system on the brain.

Furthermore, we generated a *Slco1c1-CreER* mouse line (*Slco1c1-KI-P2A-iCreERT2, briefly, Slco1c1-CreER*^{KI}). Our staining results validate its high specificity for labeling CNS endothelial cells, with rare expression in peripheral endothelial cells (Supplementary Fig. 14 and 15). *Slco1c1-CreER BAC* transgenic mouse line (*Slco1c1-CreER*^{BAC}) has been reported as the most specific line for labeling blood vessels in the central nervous system[42]. We collected results demonstrating that *Slco1c1-*

Fig. 3 | Mechanism of blood-vessel regression in the brain. a, **b** Cellular components of regressing vessels in the brain. Magenta, laminin layer stained with anti-laminin; green, endothelial cells labeled with anti-CD31; red, DsRed, pericytes in a *NG2DsRedBAC* mouse; blue, nuclei,Hoechst 33342 (HO). **c** Percentages of regressing blood vessels with different cell components: PC pericytes, EC endothelial cells, laminin, laminin layer. Inset, seven possible combinations of cell components ($n = 179$ regressive vessels). **d**, **e** In vivo imaging of regressing vessels in the brain of an adult *NG2DsRedBAC* mouse. Four types of regressing vessels were observed: I, the soma of the pericyte was located in a neighboring vessel; II, the soma of the pericyte was located at one end of the regressive vessel; III, the soma was located in the middle of the regressive vessels; IV, one end of the regressive vessel had detached from the neighboring blood vessel. **d**–**h** Time-lapse imaging of the entire process of vessel regression and pericyte fate in regressing vessels. Three different fates of pericytes (arrowheads): cell death (**f**), retention at the same location (**g**), and relocation to a neighboring vessel (**h**). Blood flow was labeled with dextran-FITC-500K. Pericytes (red, DsRed) were labeled in *NG2DsRedBAC* mice. The examples in (**f**) and Fig. 1**b** were from the same field of a mouse. **i** Summary of lifespan for 58 regressing blood vessels that were imaged ($n = 6$ mice). **j** Astrocytic endfeet around regressing vessels. Green, GFP in astrocytes from *hGFAP-GFP* transgenic mice. Endfeet (yellow arrows) of astrocytes (Ast, white arrows) enwrapped the entire surface of regressing vessels (RV, white arrowheads), which were stained with anti-laminin (red). **k** Percentages of regressing vessels fully enwrapped by astrocytic endfeet. T1–3 indicate three distinct types of regressing vessels (T1, $n = 20$ blood vessels; T2/3, $n = 14$ blood vessels). **l** Our model of vessel regression in the adult brain. Vessel regression starts with blood-flow occlusion (dark region inside the vessel) in a certain percentage of blood vessels. Endothelial cells (light green) retract rapidly in response to occlusion. Pericytes (red) remain for a long period and form a typical regressive structure with a laminin layer. Pericytes in regressing blood vessels either relocate to neighboring blood vessels or die.

CreER::Tak1$^{fl/fl}$ also induces significantly increased regression of blood vessels in the brain, similar to what we observed in *Cdh5-CreER::Tak1*$^{fl/fl}$ mice (Supplementary Fig. 16). These results are also consistent with those obtained using *Slco1c1-CreER*^{BAC}*::Tak1*$^{fl/fl}$ or *Slco1c1-CreER*^{BAC}*::Nemo*$^{fl/fl}$ in previous studies[40].

Vessel regression increases the distance between neurons and the nearest capillary

Oxygen diffusion is limited by distance, but regarding neuron accessibility to the nearest capillary. The observed vessel regression increases the distance between parenchyma and the nearest capillary. Our results indicate that this regression could potentially affect gaseous and metabolite exchange for cells in areas with the greatest increase (Fig. 6). We utilized 3D imaging of the vasculature and artificially removed regressive blood vessels, which are expected to regress over time. Using Imaris software, we measured the changes in distances from individual neurons/glial cells to the nearest blood vessels and compared the distributions before and after vessel removal. Our analysis showed a significant, albeit subtle increase in the mean distance between neurons and their nearest capillaries (from 10.96 ± 0.18 μm to 11.77 ± 0.19 μm, $n = 1563$ cells). Notably, the proportion of cells that were furthest from blood vessels (>30 μm) doubled (from 0.32% to 0.64%) after vessel regression. Additionally, a fraction of neurons in the second furthest group also showed a noticeable increase (from 13.82% to 17.21%) (Fig. 6).

Remarkably, we observed a significant increase in the distance between a brain cell and the nearest blood vessels in the brains of *Tak1 CKO* mice (WT: 5.80 ± 0.07 μm, $n = 2961$ cells, *Tak1*$^{AAV\text{-}BRI\text{-}Cre}$: 10.05 ± 0.13 μm, $n = 1716$ cells, *Slco1c1-CreER*^{KI}*::Tak1*$^{fl/fl}$: 11.72 ± 0.18 μm, $n = 1994$ cells, Fig. 7).

Vessel regression leads to abnormalities in neuronal metabolism and glutamate production

To determine whether the reduction of neuronal activity in the brains of *Tak1 CKO* mice was due to neuronal degeneration, we stained neurons with Fluro Jade C[26], a marker for all degenerating neurons regardless of specific insult or mechanism of cell death. We did not detect degenerating neurons in brain sections of *Tak1 CKO* mice. Similar results were observed when we stained neurons with the antibodies against activated caspase-3, a marker for apoptotic cells. We performed co-staining of brain sections with TUNEL and antibodies against NeuN. The brain samples were collected 1–2 weeks after tamoxifen administration to *Tak1 CKO* mice. We did not observe degenerating neurons near the regressing vessels ($n = 120$ regressing vessels, see example images below) in *Tak1 CKO* mice (Supplementary Fig. 17).

We further asked whether the accumulation of regressive vessels in *Tak1 CKO* results in mitochondrial dysfunction and affects energy generation in neurons. We performed electron microscopy (EM) to image brain sections from the cerebral cortex of control and *Tak1 CKO* mice. Mitochondria from neuronal synaptic terminals of the control and *Tak1 CKO* brains were compared, and we observed that mitochondria in the neurons of *Tak1 CKO* mice had abnormal morphology. Specifically, the cristae showed irregular morphologies and lower electrical signals under EM. The number of cristae decreased and they were unevenly distributed in the synaptic mitochondria of *Tak1 CKO* brains (WT or *Tak1*$^{fl/fl}$, $n = 23$ mitochondria; *Tak1 CKO*, $n = 17$ mitochondria, Fig. 8a, b).

To further determine whether the abnormalities in mitochondria affected metabolic pathways involved in energy generation in the brain, we collected tissues from the cerebral cortex of control (Ctrl, WT or *Tak1*$^{fl/fl}$, $n = 5$ mice) and *Tak1 CKO* mice ($n = 5$ mice) for targeted metabolomic analyses and RNA sequencing. We measured over 200 metabolites for the metabolomic analysis, including 20 amino acids and their derivatives. These measurements covered most metabolites of the classical metabolic pathways in cells[43]. The metabolite profiles from the control and *Tak1 CKO* brains tended to cluster separately in unsupervised principal component analysis (PCA) (Fig. 8c), indicating dramatic alterations in metabolomes between control and *Tak1 CKO* brains (Fig. 8c). Among the metabolites that we detected, pyruvate, α-ketoglutarate (α-KG), fumarate, and NAD^+ were significantly decreased in *Tak1 CKO* brains (Fig. 8d–f). These metabolites are crucial for the TCA cycle and energy generation pathways, which is consistent with the morphological abnormality that we observed in mitochondria. In addition, we detected the glutamate concentration was much lower in *Tak1 CKO* compared to the control group (69.1 ± 5.9%, $n = 5$ in control and *Tak1 CKO* brains). The concentration was normalized to that of the control group. ($n = 5$ in control and *Tak1 CKO* brains, Fig. 8d–f). In addition, we also detected valine, kynurenine, carnitine, phosphoserine, and guanidoacetic acid etc were significantly increased in *Tak1 CKO* brains (Supplementary Fig. 18)

Our further RNA sequencing analysis showed that a gene cluster pertaining to glutamatergic transmission was downregulated in *Tak1 CKO* mice. The expression levels of the genes (e.g., *Plcb2, Gnas, Plcb3, Pla2g4a*, etc.; Fig. 8g, h) associated with the glutamatergic synapse dramatically decreased (Fig. 8g–i). In addition, we observed that the expression levels of some glutamate receptor-encoding genes (e.g., *Grik5, Grin2a, Gria1*, etc.; Fig. 8i) significantly increased, their upregulation might be a compensatory response to a decrease in available glutamate to some extent. Our results from both transcriptome and metabolomic measurements, as well as EM imaging, demonstrated that increasing vessel regression led to an alteration of the neuronal metabolism (i.e., energy generation and glutamate metabolism), and as a result, decreased the activity in neurons. Given that it is extremely difficult for us to isolate the contribution of energy production and synaptic transmission to the reduction of neuronal activity in *Tak1 CKO* mice, further investigation with new methods/tools is required to continue this study in the future.

https://doi.org/10.1038/s41467-025-60308-0

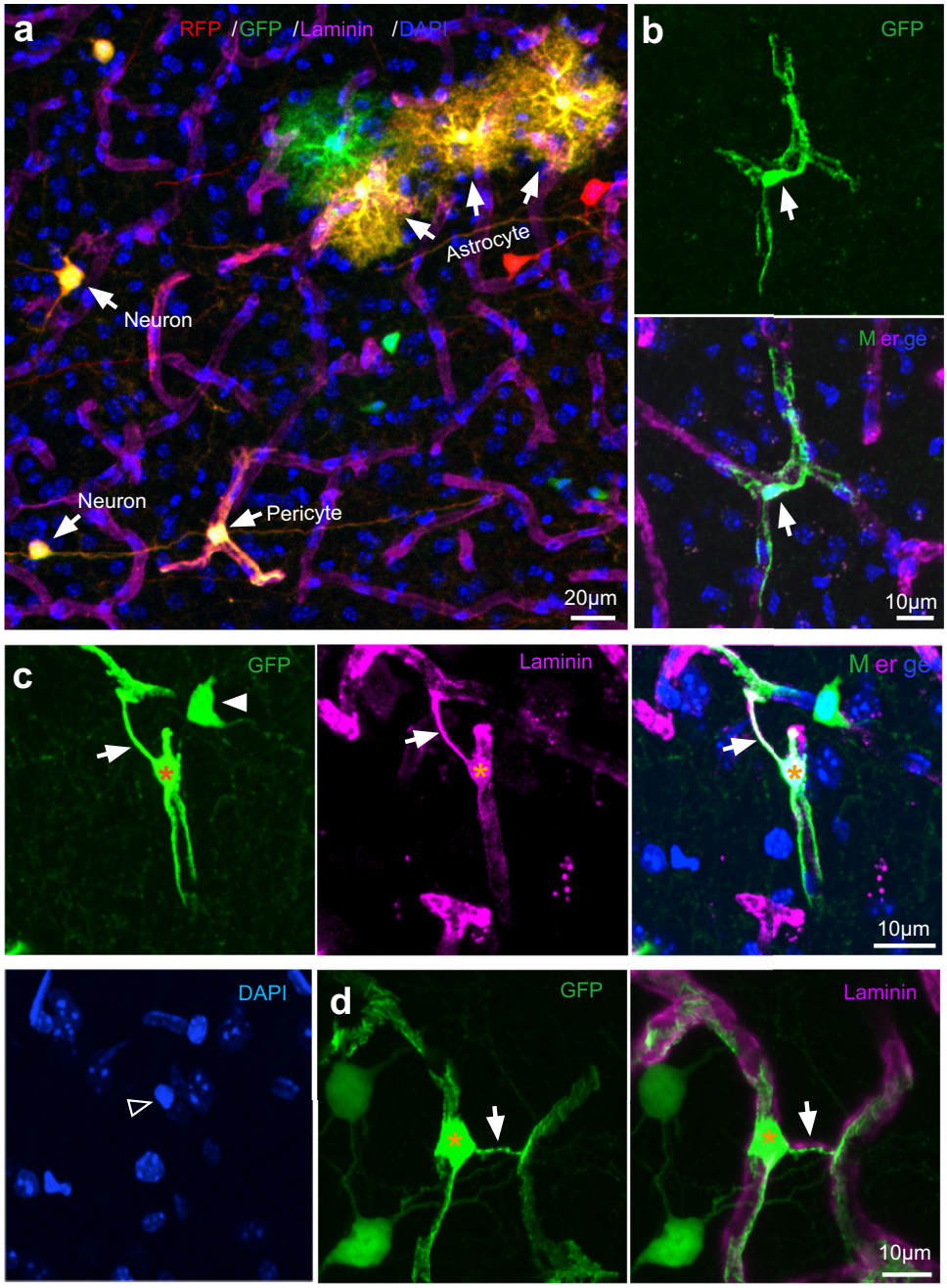

Fig. 4 | Morphology of pericytes in regressing vessels. a An example image of a brain section of a *Hprt-Cre::MADM* mouse. Neurons and glial cells are labeled, and pericytes were sparsely labeled (arrows). **b** Morphology of a typical pericyte. **c**, **d** Gross morphology of an individual pericyte from a regressing vessel in the brain of a *Hprt-Cre::MADM* mouse. Arrows, regressing vessels. Asterisks indicate the somas of the pericyte in regressing vessels. The processes extending from pericytes on both blood vessels were very complex, indicating a stable structure. A neuron (white arrowhead) is close to the pericyte (with its nucleus, hollow arrowhead) in **c**. Purple, signal from anti-laminin; blue, nuclei labeled with DAPI; red, red fluorescence protein (RFP); green, GFP.

Previous studies have indicated that pericyte integrity is crucial for neuronal survival via secretion of pericyte-specific factors[44]. To investigator whether neuronal metabolic dysfunction in their models is also caused by reduced neurotrophic support by the neurovascular unit, we analyzed the pericyte-specific factor PTN from our bulk-seq results, and no difference in its expression was observed between the wild-type and *Tak1 CKO* groups (Supplementary Fig. 19). We also did some data mining at https://tabula-muris.ds.czbiohub.org/, and realized that some glial cells also have high *Ptn* expression. Because we performed bulk RNA sequencing of the whole tissue, our results might underestimate the *Ptn* expression alterations in pericytes because *Tak1* was only removed from endothelial cells in *Tak1 CKO* mice. In addition to *Ptn*, we also examined other neurotrophic factors, including *Bdnf*, *Gdnf*, *Ntf3*, and *Vegfa/b*, and found no significant difference in their expression between wild-type and *Tak1 CKO*.

Discussion

The term "brain plasticity" usually refers specifically to neuroplasticity because neurons are the most functionally relevant cell type in the brain[45]. Our data indicate that the blood-vessel pattern in the mature adult mammalian brain changes substantially with age. VEGF is a critical molecule for both vessel development and regression[22,46]. Genetic alteration of VEGF-R2 promotes vessel recanalization and minimizes

https://doi.org/10.1038/s41467-025-60308-0

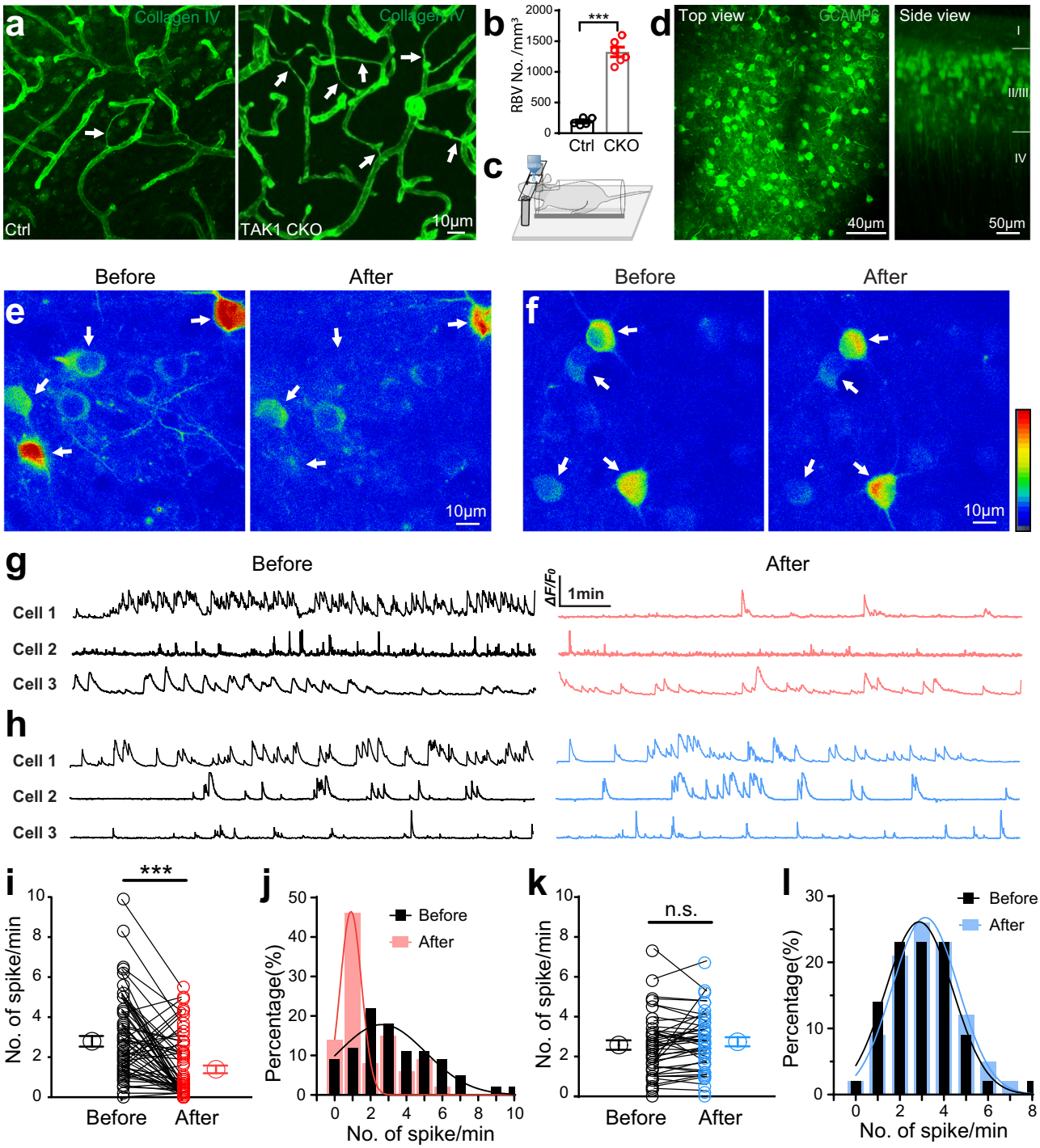

Fig. 5 | In vivo imaging of neuronal activity in *Cdh5-CreER:Tak1$^{fl/fl}$* mice. **a** Example images of blood vessels in brain sections from control (Ctrl) or *Cdh5-CreER::Tak1$^{fl/fl}$* (*Tak1 CKO*) mice.White arrows, regressive blood vessels. **b** Statistical analysis of the density of regressive blood vessels in the brain of *Tak1 CKO* and control mice (Ctrl, $n = 5$ mice; *CKO*, $n = 6$ mice). ***$p < 0.001$, Student's *t*-test, error bars indicate SEM. **c** Strategy used to image neuronal activity in the brain of conscious mice. **d** GCaMP6 signal of neurons in layers II–IV of the cerebral cortex. *AAV-CAMKII-GCaMP6m* was injected ~1 month before imaging. I–IV, cortical layers. Example images of the GCaMP6 signal obtained from *Tak1 CKO* (**e**) and control mice (**f**) before and after administration of tamoxifen. Warm pseudocolor indicates a high calcium signal. Representative traces of calcium transients recorded from three neurons (arrows) of a *Tak1 CKO* mouse (**g**) and a control mouse (**h**) before and after a 1-week administration of tamoxifen. **i** Statistical analysis reveals the significance of differences of calcium transients in *CKO* mice as shown in (**e**) and (**g**). Each connected pair of black and red circles denotes data obtained with the same neuron before (black) and after (red) tamoxifen injection. Each of the two large circles denotes the mean ± SEM for the two groups. ***$p < 0.001$, paired Student's *t*-test. **j** Frequency distribution of calcium transients from all neurons before (black) and after (red) tamoxifen was administered. Red Gaussian curve shows that the spike frequency was shifted to the left (i.e., lower value) after injection of tamoxifen into *Tak1 CKO* mice ($n = 65$ neurons from 5 mice). **k** No significant differences (n.s.) of calcium transients observed in control mice as shown in (**f**) and (**h**). Each connected pair of black and blue circles denotes data obtained with the same neuron before (black) and after (blue) tamoxifen injection. Each of the two large circles denotes the mean ± SEM for the two groups, two-tailed *t*-tests. **l** Frequency distribution of calcium transients from all neurons before (black) and after (blue) tamoxifen solution was administered. The Gaussian curve shows that the spike frequency was not shifted after injection of tamoxifen into control mice (*Tak1$^{fl/fl}$*). $n = 43$ neurons from 5 mice.

https://doi.org/10.1038/s41467-025-60308-0

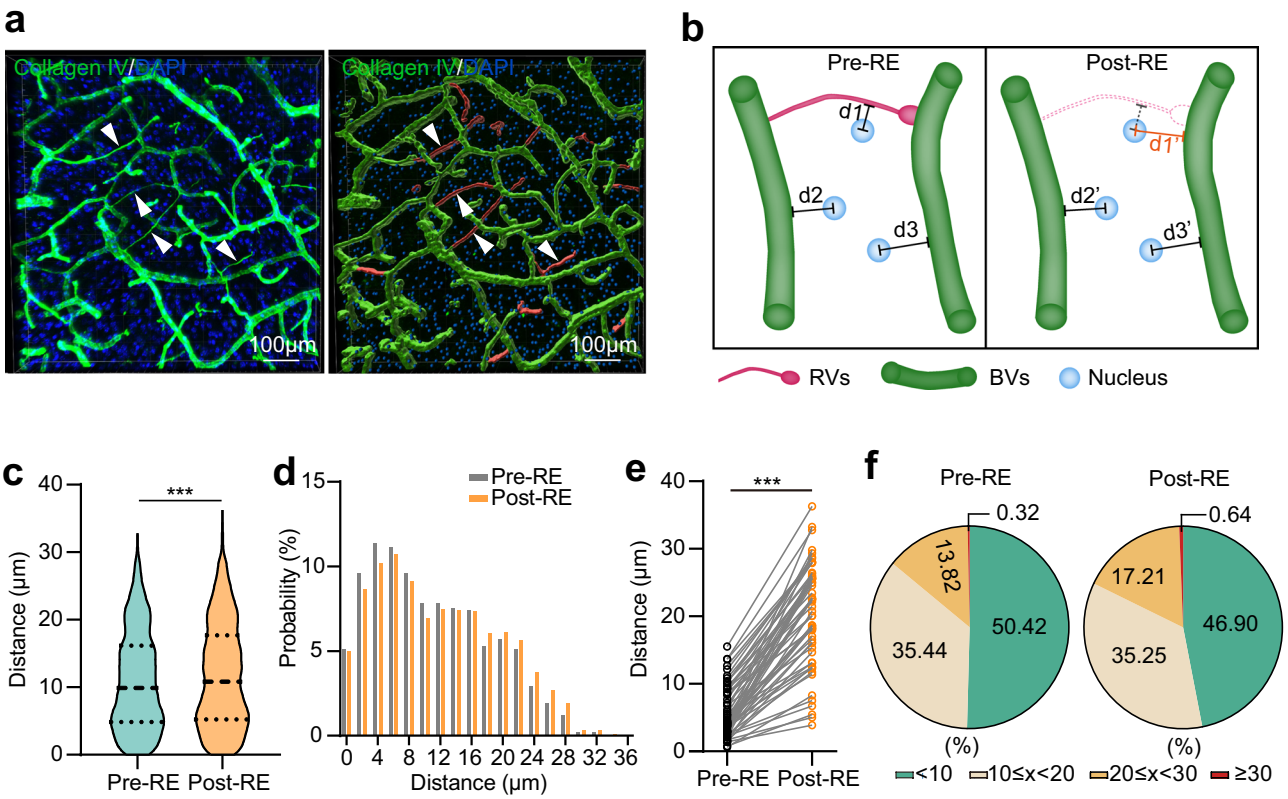

Fig. 6 | Analysis of the distance between cells and their nearest blood vessels in the retinal vascular system. a Simulated image (right) of cortex blood vessels (left). Blood vessels were stained with anti-Collagen IV, and cell nuclei were stained with DAPI. Reference images (left) were stacks of images from brain sections. **b** A schematic illustrating the strategy used to analyze the shortest distance between cells and blood vessels before (Pre-RE) and after (Post-RE) removing regressive vessels. **c** Distribution of the shortest distance from the nucleus to blood vessels ($d_{n\text{-}v}$) before and after removing regressive vessels (Pre-RE and Post-RE, $n = 1{,}563$ cells from one mouse retina sample). **d** Probability distribution of $d_{n\text{-}v}$ before and after removing regressive vessels (Pre-RE and Post-RE). **e** Changes in $d_{n\text{-}v}$ distances before and after removing regressive vessels. The figure shows only the $d_{n\text{-}v}$ distribution with a ratio of $d_{n\text{-}v}$ (Post-RE)/$d_{n\text{-}v}$ (Pre-RE) greater than 1. **f** Percentage of cells grouped by $d_{n\text{-}v}$ distances (group 1: $d_{n\text{-}v} < 10$ μm; group 2: 10 μm ≤ $d_{n\text{-}v} < 20$μm; group 3: 20≤$d_{n\text{-}v} < 30$μm; group 4: $dn_{\text{-}v} \geq 30$μm) before and after removing regressive vessels. ***$p < 0.001$, two-tailed paired t-test.

their pruning[46]. In the human brain, the responsiveness of HIF1 to hypoxia wanes with age, thereby reducing *VEGF* expression[47,48].

The plasticity of brain vasculature reflects various processes. Over the long term, we believe that angiogenesis (resulting in an increase in blood vessel density) and regression (resulting in a decrease in blood vessel density) represent two complementary aspects of vessel plasticity in the brain. Angiogenesis is highly active in the brain during the early postnatal period, particularly between P5–10. Newly formed vessels are more than regressed vessels; thus, we detect the increase of blood vessels in the brain before P21. From time-lapse in-vivo imaging results, we observed that angiogenesis is rarely detected in the brains of mice aged 2–4 months. This finding is consistent with our previous research, where we rarely observed proliferating endothelial cells (EdU^+) in the adult brain[49]. In contrast, vessel regression remains active throughout adulthood, including the adult and aging stages (a regression rate of 0.34% per week, or 1.72% over 5 weeks). As a result, the density of brain vasculature decreases, although it is very slow (Supplementary Fig. 20). We conclude (at this stage rather speculatively) that regression is likely to contribute to the decrease in vessel density. However, we currently lack direct evidence to prove this hypothesis. Advancements in technology in the future may allow researchers to trace brain vasculature in large fields of view in the same mouse over the course of several months in a non-invasive manner, providing a clear picture of the alteration of blood vessels in the adult brain.

The plasticity may also exist in the pericyte coverage in the brains of mice at different ages. Following the methodology outlined in a previous study, brain sections from mice aged 2, 7, and 21 months were stained with antibodies against PDGFRβ and GluT1 for labeling pericytes and endothelial cells, respectively. Consistent with findings from the previous results[44], we observed a decrease in pericyte coverage over time (Supplementary Fig. 21).

Our live-imaging experiments only rarely revealed new vessel formation in the adult mouse brain under physiological conditions. Accumulation of regressive vessels (our estimate: ~20% per year in the mouse brain) might explain the dramatic reduction of blood vessels in the adult mammalian brain.

The distance over which oxygen can diffuse in the normal brain is highly regulated. The limit of oxygen diffusion is 100–150 μm in live tissue[50,51]. The distance between capillaries is ~40 μm in mice[52]. In the white matter of the human brain, the capillary density is much lower than in the gray matter, and the inter-capillary distance can reach 100 μm. Vessel regression leads to a decrease in blood-vessel density and causes the inter-capillary distance to exceed the limit of oxygen diffusion, and the consequent reduction of oxygen availability to brain cells may result in stress on neurons or glial cells during periods of increased activity in a particular brain region; this may explain why the chronic low-grade ischemia caused by hyaline arteriolosclerosis (hypertension-induced disease of brain arterioles) or chronic cerebral hypoperfusion preferentially damages the white rather than the gray matter[53], ultimately resulting in a diminution of the vasculature with consequent dementia.

It has been reported that alteration of neuronal activity causes remodeling of blood vessel patterns in the brain[54]. Both endothelial

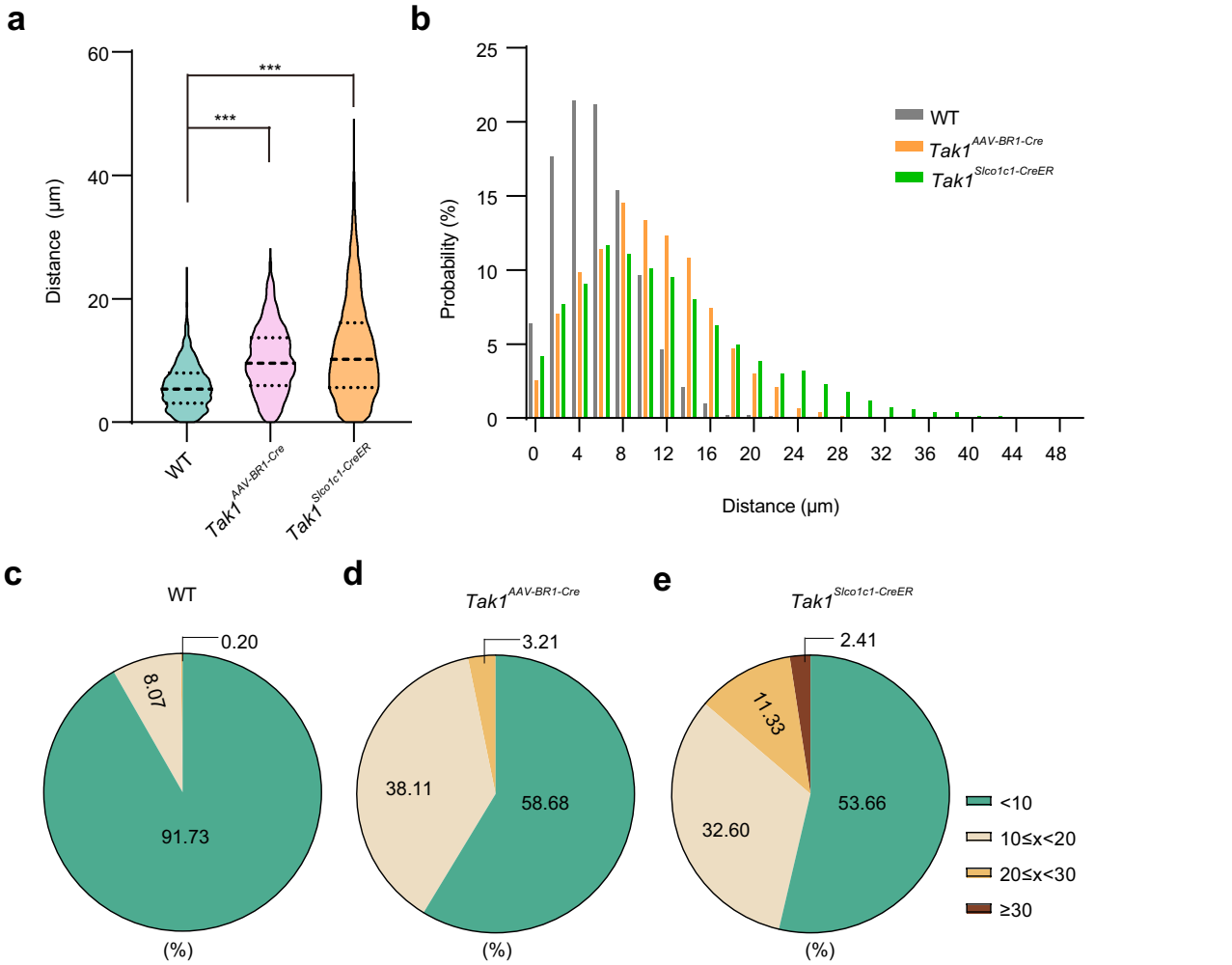

Fig. 7 | Analysis of the distance between cells and their nearest blood vessels in the brain with *Tak1* deletion. a Distribution of the shortest distance from cells to blood vessels ($d_{n\text{-}v}$) in wild-type (WT, $n = 2961$ cells from one mouse brain slice) mice and two groups of *Tak1 CKO* mice: group 1 (*Tak1*$^{AAV\text{-}BR1\text{-}Cre}$, *AAV-BR1-Cre* injected into *Tak1*$^{fl/fl}$ mouse, n = 1716 cells from one mouse brain slice) and group 2 (*Tak1*$^{Slco1c1\text{-}CreER}$, *Slco1c1-CreER*^{KI}::*Tak1*$^{fl/fl}$, n = 1994 cells from one mouse brain slice). **b** Probability distribution of $d_{n\text{-}v}$ in the brain of WT and the two *Tak1 CKO* groups. Percentage of cells grouped by $d_{n\text{-}v}$ distances for WT (**c**), *Tak1*$^{AAV\text{-}BR1\text{-}Cre}$ (**d**), and *Tak1*$^{Slco1c1\text{-}CreER}$ (**e**). ***$p<0.001$, two-tailed unpaired *t*-test.

cells and pericytes play an active role in the functional coupling of the neurovascular unit, in which blood vessels are the key component[5,12,55]. Any dramatic alterations (remodeling, regression, angiogenesis, etc.) in the pattern of the brain vasculature may result in altered regulation of brain microcirculation, which in turn is likely to lead to changes in the local supply of glucose and oxygen in the brain[6,11,56]. Neurons are the key player in brain function, and they consume the most glucose and oxygen in the adult mammalian brain[3]. After an alteration to the microcirculation, especially a decrease in blood supply followed by vessel regression, neurons will be the most vulnerable cell type under these stressed conditions, and they will sustain damage[57]. Although we detected a substantial decrease in neuronal activity in the cerebral cortex in *Tak1 CKO* mice due to an increasing accumulation of regressive vessels, further work is required to determine how blood vessel regression regulates energy-related metabolism under physiological conditions and whether a certain threshold of vessel regression leads to neuronal or synaptic degeneration.

Capillary rarefaction in *Tak1 CKO* mice is greater, more synchronous, and faster than in WT mice. Thus, while capillary rarefaction may contribute to neuronal dysfunction in *Tak1 CKO* mice, it is unclear if the same applies to WT mice. Given the low percentage of blood vessels entering the regression process under physiological conditions, it becomes exceedingly difficult for researchers to accurately assess the significance of vessel regression in this context. To address this challenge, we have opted to amplify vessel regression using *Tak1 CKO* mice and investigate its impact on neuronal activity and synaptic function. However, we acknowledge that it remains unclear whether the observed effects are applicable to wild-type mice, despite the defects observed in neuronal activity and synaptic functions. This design is a limitation of our study. We hope that future researchers in the field of regression will provide better strategies or utilize new technologies to address these fundamental questions more effectively.

Methods

Animals

All rodent experiments were conducted in accordance with protocols approved by the Institutional Animal Care and Use Committee at at Chinese Institute for Brain Research (No. IACUC-040), Beijing, and the University of Texas Southwestern Medical Center. Rearing conditions: constant temperature (24 °C), constant humidity (40–60%), 12 h light (lights on at 8 am, lights off at 8 pm). Water and food are freely available 24 h a day, and clean cages and bedding are replaced weekly. *MADM* mouse strain was originally from Dr. Liqun Luo lab at Stanford (also available from Jackson lab, Cat# 021457). The GT/TG locus is located on Ch7. *Hprt-Cre* mouse line was from Jackson lab (Cat# 004302). *Tak1*$^{fl/fl}$ mouse line was purchased from Jackson Lab (Cat# 011038).

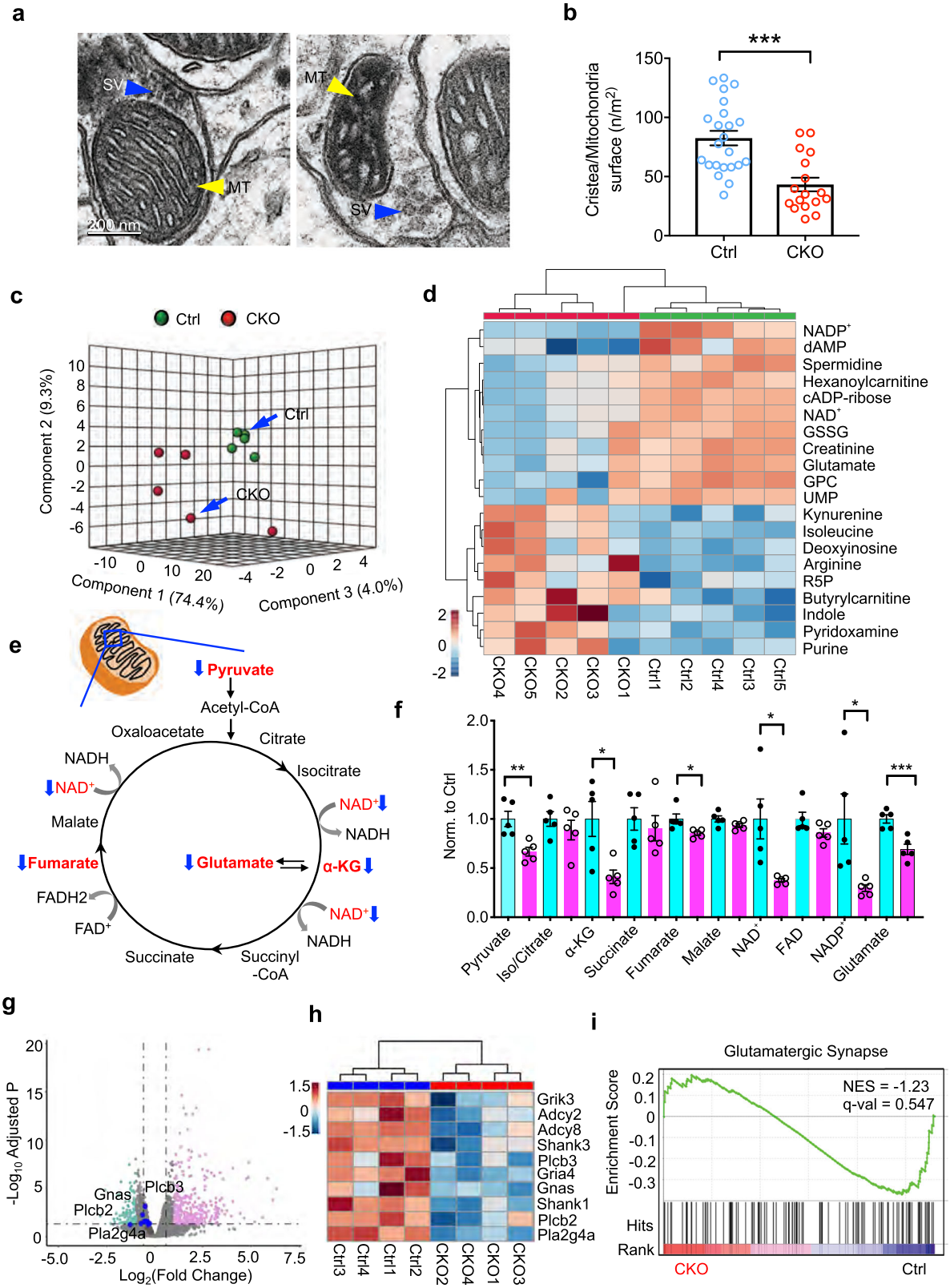

NG2DsRedBAC was originally from the Akiko Nishiyama lab (also available at the Jackson lab, Cat# 008241). *Pdgfrb-Cre* from Volkhard Lindner's lab. *Cdh5-CreER* was from Ralf H. Adams's lab. *Ai14* and *Ai6* are available from the Jackson lab (Cat# 007908 for *Ai14* and 007906 for *Ai6*). Both male and female mice were used in the experiments, unless otherwise specified. The animals were anesthetized with isoflurane, and euthanasia was performed using either carbon dioxide or Avertin.

In vivo labeling of brain microcirculation

Fluorescein isothiocyanate-Dextran 500,000-Conjugate (FITC-Dextran, Sigma Aldrich) or TRITC-dextran (Sigma Aldrich) was prepared in saline (0.9% NaCl) at a concentration of 10 mg/ml. Adult mice were anesthetized with a mixture of ketamine (80–100 mg/kg) and xylazine (10–12 mg/kg). The tail was warmed with a heat lamp for about 1 min and then wiped with 70% ethanol around the injection site. A 31 G

Fig. 8 | Abnormalities of neuronal metabolism in the brains of *Tak1 CKO* mice. **a** The morphology of mitochondria in synapses from control and *Tak1 CKO* mice (*Cdh5-CreER::Tak1$^{fl/fl}$*). SV, synaptic vesicles. MT, mitochondria. **b** Summarized results (mean ± SEM) of mitochondrial features in control and *Tak1 CKO* mice. Y-axis, the number of cristae was normalized to the surface of mitochondria. ***, $p < 0.005$, unpaired Student's *t*-test. **c** Principal component analysis (PCA) of the metabolomes of control (Ctrl) and *Tak1 CKO* samples. **d** A heatmap representation of 20 metabolites (VIP score > 1, i.e., Variable Importance in Projection) in the cerebral cortex of five control (Ctrl) and five *Tak1 CKO* mouse brains. Color bar (bottom left) indicates the scale of standardized metabolite levels. Warm color indicates higher concentration. NAD^+ Nicotinamide adenine dinucleotide; dAMP deoxyadenosine monophosphate; GSSG oxidized glutathione; GPC Glycerophosphocholine; R5P Ribose 5-phosphate (Ctrl group, $n = 5$ mice; *CKO* group, $n = 5$ mice). **e**, **f** Schematic illustrating all metabolites in the tricarboxylic acid cycle (TCA). Blue arrows indicate a decrease of these metabolites (highlighted in red) in *Tak1 CKO* mouse brains. Metabolites without arrows (black), no significant difference. Relative abundance (normalized by TIC of the control group) of the metabolites shown in **e** from control (light blue) and *Tak1 CKO* (magenta) samples. *, $p < 0.05$, **, $p < 0.01$, ***, $p < 0.005$; two-tailed unpaired Student's *t*-test. FAD, flavin adenine dinucleotide. **g** Volcano plot representing significantly up- and down-regulated genes. *Padj*, adjusted *p* value. Ctrl ($n = 4$ mice) and *Tak1 CKO* ($n = 4$ mice). Up-regulated and down-regulated genes are highlighted in pink and light blue, respectively. Core genes in the "Glutamatergic Synapse" gene set are in bold; blue represents genes with significant differential expression, while brown represents genes with no significant difference, two-tailed *t*-tests. **h** Color scale heatmap showing the normalized expression of core genes of the Glutamatergic Synapse gene set, which is significantly down-regulated in the *Tak1 CKO* group vs Ctrl. **i** GSEA plots of Glutamatergic Synapse gene set, with black bars indicating gene sets represented among all genes pre-ranked by ranking metrics (Ctrl versus *Tak1 CKO*), with indicated normalized enrichment score (NES) and false discovery rate (FDR) q-value.

insulin syringe needle was inserted with the bevel up, at an angle of 5–15 degrees, into the vein. 80–100 µl FITC-dextran 500 K Da solution was injected. Blood circulation could then be detected via the FITC signal, and blood cells were visualized by contrast as dark areas without a fluorescent signal.

Fluorescent labeling of blood cells

Labeling was conducted as previously reported with some modifications[26]. Briefly, 30–100 µl of blood (2–4 drops) was taken from the submandibular veins of the mouse after poking its cheek with a Goldenrod animal bleeding lancet. The blood was collected in an Eppendorf tube containing 500 µl of 1× Hank's Balanced Salt Solution (HBSS) with 10 mM EDTA added as an anticoagulant. The whole blood was centrifuged at 150 g for 3 min. After the supernatant was removed, the pellet was resuspended in 1 ml HBSS containing DiO (7 µM, Thermofisher Scientific). Cells were then incubated at 37 °C for 15 min. Labeled blood cells were washed twice with HBSS and then centrifuged and resuspended in 300 µl HBSS. About 50 µl solution with DiO-labeled cells was injected back to the same mouse through the tail vein. DiO dye was excited with a laser at 488 nm or 860 nm IR-laser on Zeiss LSM710.

Longitudinal time-lapse imaging of brain vasculature in vivo

Glass cranial windows were made in the skulls of different transgenic mice, allowing 1–2 months recovery from the craniotomy surgery before we performed live imaging on an upright Zeiss LSM710 NLO two-photon excitation microscope with a 20×/1.0 water-immersion objective lens (Zeiss). Regions of interest (ROI) were scanned with XYZ mode for time-lapse imaging as we previously reported[26,58]. The same ROI area was re-located using the branching pattern of major blood vessels, and Z-stack images were scanned once a week (1–2 h) in the following 1–6 months. We measured the speed of blood flow in the visualized vessels with the line scanning function. During imaging, mice were anaesthetized with 1–2% isoflurane in oxygen, and their body temperature was kept with a home-made heating pad (10 × 5 cm). Blood vessels were visualized by FITC–dextran injected through mouse the tail vein in *NG2DsRedBAC* tg mice. Blood vessels in the brains of *Cdh5-CreER::Ai6::NG2DsRedBAC* triple transgenic mice were visualized by TRITC-dextran. DsRed, FITC, or ZsGreen was excited with IR laser (930–960 nm for DsRed, 860 nm for FITC/ZsGreen) or one photon laser (543 nm for DsRed, 488 nm for FITC/ZsGreen).

In vivo imaging of neuronal activity in conscious mice

AAV-CAMKII-GCaMP6m (in 0.5 µl phosphate-buffered saline with a titer of 2.4×10^{12}) was injected into layers II–IV of the cerebral cortex of mice at the age of 8–10 weeks. A glass cranial window was built using the same surgery procedure described above for longitudinal time-lapse imaging. We usually measured the GCaMP6 signal approximately 20–30 days post-injection of AAV from layers II–IV around the injection site in *Cdh5-CreER::Tak1$^{fl/fl}$* mice. Tamoxifen (Sigma, Cat# T5648) was administered intraperitoneally (70 µg/kg body weight; 10 mg/ml tamoxifen was dissolved in a mixed solution of corn oil and ethanol, 9:1 v/v). A two-photon laser (950 nm) was used to image GCaMP transients 200–700 µm below the pia in conscious mice with a 20× water immersion lens (N.A., 1.0) mounted in a Zeiss LSM780 microscope (setting, 512 × 512, frequency 5 Hz, for 10 min). Images were processed with Image J to generate the ΔF/F curve as described[59]. Briefly, the fluorescence density of each ROI (region of interest) time series was measured, with the baseline fluorescence (F_O) being defined as the average of the lowest 10% of samples. The instantaneous fluorescence of the ROI time series is F, and $\Delta F = F - F_0$. The 100 × ΔF/F curve was plotted using Clampfit 10.0 software. The frequency of GCaMP-mediated calcium transients was detected with MiniAnalysis software. Quantitative data were processed with GraphPad Prism software, and statistical analysis was carried out with the Student's *t*-test.

We utilized home-made software, which Hui Lu laboratory developed for motion corrections. This software is frequently used for in vivo neuronal imaging in conscious animals, coupled with simultaneous motor behavior analysis[60,61].

Immunostaining

The use of human brain tissue from patients for immunostaining was approved by the Institutional Review Board at Fujian Medical University Union Hospital (No. 2022WSJK008), Capital Medical University (No. SBNK-YJ-2023-021-02), and the University of California, San Francisco (No. 28913-BU-01-BAC) as part of the study. Consent was obtained for biospecimen collection. Ethical guidelines were followed. The use of brain tissue from non-human primates was approved by the Institutional Animal Care and Use Committee of the Institute of Biophysics of the Chinese Academy of Sciences (No. N-W-20131104).

Mice of different ages were perfused transcardially with 20 ml of PBS, followed by 20 ml of 4% (w/v) paraformaldehyde (PFA) in PBS. The brain was fixed in cold PFA at 4 °C for 1.5–2 h, washed with a large volume of PBS overnight at 4 °C, and dehydrated with 15% and 30% sucrose in PBS sequentially. The human brain was fixed whole in 20% formalin for 9 days and then dissected, showing no gross abnormalities; samples were taken from the frontal lobe cortex with subcortical white matter, cerebellum, hippocampus, and basal ganglia (caudate and putamen). The decedent was a 45-year-old man who died from the complications of disseminated neurodendocrine carcinoma of the pancreas; the permission to use tissue for research was covered by the autopsy permit signed by his next-of-kin. Fixed mouse brains and monkey or human brain samples were sectioned with a cryostat (model CM3050S, Leica) or a vibratome (Leica) into sections of 20–70 µm thickness. Sections were permeabilized with 0.25% Triton X-100 and then blocked with 5% BSA and 3% normal goat

serum with 0.125% Triton X-100 for 2 h. Primary antibodies against mouse or human laminin (1:300 rabbit, Sigma, No. L9393), mouse collagen IV (1:300, rabbit, EMD Millipore, No. AB756P), mouse CD31 (1:300, rat, BD Pharmingen, BD550274), or mouse PDGFRβ/CD140b (1:300, rat, eBioscience, No.14-1402-81) were incubated with brain sections for 24–48 h at 4 °C. Together with Hoechst33342 or DAPI (1 μg/ml), secondary antibodies conjugated with Alexa488, 546 or 647 (1:500, Life Technologies) were used after 2 h incubation at RT (22–25 °C). Sections were mounted with anti-fade mounting medium Fluoro-Gel (EMS). All images were taken with a Zeiss LSM710 NLO confocal microscope. Whole-section images were scanned with the tiling function on an inverted Zeiss LSM780 confocal microscope, with a 20×/0.8 air objective lens or 63×/1.4 oil objective lens.

Counting of regressive vessels

Regressive vessels (RV) are very thin, typically measuring only 1–2 μm in diameter. They cannot be automatically recognized by software, requiring a highly experienced lab member to manually identify them from high-resolution images. This process usually takes a lab member 3–4 days to count and measure the length of all regressive vessels from a single brain slice with a thickness of 50–80 μm. While this task is time-consuming, it ensures accuracy compared to using commercial software, which cannot reliably identify these vessels. To ensure consistency, we typically have a second lab member double-check all labeled regressive vessels in Imaris 10.0 to ensure both members are using the same criteria. For quantification from 3D images, we also manually measure RVs, but capillaries can be measured automatically with Imaris, with manual correction if any tracing errors are detected.

Tissue clearing with PEGASOS

Thick slices were cleared as previously[62]. Briefly, immunostaining (1st antibody, anti-collagen IV, 1:300, incubation time, 7 d; 2nd antibody, Alexa 488, 1:500, incubation time, 3 d at 4 °C) was performed before we started the tissue clearing. Brain slices (500 μm) were then treated with Quadrol decolorization solution for 2 d at 37 °C after fixation with 4% PFA solution for 24 h. Samples were then immersed in gradient delipidation solutions in a 37 °C shaker for 1 to 2 d, followed by dehydration solution treatment for 1 to 2 d and BB-PEG clearing medium treatment for at least 1 d until reaching transparency. Slices were then preserved in the clearing medium at RT before imaging with a confocal microscope (Zeiss LSM780).

Image data analysis

Image data analysis was done with Image J software (NIH) and ZEN image processing software from Zeiss. The number of regressing vessels (RV) was counted manually with ZEN software. RV density per square millimeter was normalized from the optical volume of the images. The blood vessel length density (Fig. 3) was measured by calculating the area of all blood vessels from 3-D projection images in Image J. 3D reconstruction and movies of 3D blood vessels and RV distribution (Supplementary Video 5) were produced with Imaris 10.0 (Bitplane).

Imaging mitochondria with electron microscopy

The subcellular mitochondrial morphology and synaptic structure were imaged using electron microscopy (EM). On days 7–10 after tamoxifen injection at 12-14 weeks old, *Cdh5-CreER::Tak1$^{fl/fl}$* and their littermates (control mice) were anesthetized and transcardially perfused with EM fixation solution (4% PFA in 0.1 M sodium cacodylate buffer, pH 7.4, containing 0.1% glutaraldehyde) at room temperature. The brain was collected and then fixed in solution (2.5% glutaraldehyde in 0.1 M Sodium Cacodylate Buffer, pH 7.4) for 2 h at 4 °C. 1 mm cubic blocks of cortical tissue and hippocampus tissue were collected and embedded in resin embedding medium (Epon). Blocks were sectioned with a diamond blade (Diatome) on a Leica Ultracut 7 ultramicrotome (Leica Microsystems) and collected onto copper grids. Thin sections were negatively stained with 2% aqueous uranyl acetate. Images were acquired using a Morada Digital Camera and iTEM software (Olympus) under an FEI Tecnai G2 Spirit Biotwin transmission electron microscope, at a voltage of 120 KV. Quantitative data and statistical analysis were processed in GraphPad Prism 9.0 software and ImageJ.

Purification of metabolites from brain tissue

Cortical tissue samples from the rostral hemisphere (1/2 of the cortical region of the whole hemisphere) were collected in an Eppendorf tube, and then 2 ml ice-cold 80% methanol/20% water (vol/vol) was added before weighing. The samples were homogenized and vortexed for 5 min. We transferred the extracted solution with 5 mg of brain tissue to 900 μl ice-cold 80% methanol/20% water (vol/vol) and vortexed for 1 min. After centrifugation at 17,000 *g* for 15 min at 4 °C, 800 μl of the supernatant was transferred to a new tube. All samples were evaporated until dry using a SpeedVac concentrator (Thermo Savant). The samples were stored under −80 °C before we performed targeted metabolomic measurement.

Targeted metabolomics and data analysis

Metabolites extracted from the cerebral cortex were reconstituted in 50 μl 0.03% formic acid in water and then analyzed with a SCIEX QTRAP 5500 liquid chromatograph/triple quadrupole mass spectrometer as done in our previous study[43,63]. Using a Nexera Ultra-High-Performance Liquid Chromatograph system (Shimadzu Corporation), we achieved separation on a Phenomenex Synergi Polar-RP HPLC column (150 × 2 mm, 4 μm, 80 Å). The mass spectrometer was used with an electrospray ionization (ESI) source in multiple reaction monitoring (MRM) mode. We set the flow rate to 0.5 ml/min and the injection volume 20 μl. We acquired MRM data with Analyst 1.6.3 software (SCIEX). A total of 204 metabolites were measured from each sample, and all detected metabolites were used for PCA. We have included a table containing the transitions of all metabolites presented in Fig. 8 for reference (Supplementary Table 1).

Metabolomics data analysis

Integrated chromatogram peaks of each metabolite were analyzed with MultiQuant software (AB Sciex). The ion intensity was calculated by normalizing single ion values against the total ion value of the entire chromatogram (i.e., Total Ion Chromatogram/TIC)[63]. The data matrix was input into SIMCA-P software (Umetrics) by mean-centering and Pareto scaling for subsequent analysis so that the model fitting would not be biased by concentrations and variations of different metabolites[43]. Both unsupervised and supervised multivariate data analysis approaches including principal component analysis (PCA), were performed using Metaboanalyst 4.0[64]. All data are presented as mean ± SEM.

RNA sequencing (RNA-Seq) and differential expression analysis

Cdh5-CreER::Tak1$^{fl/fl}$ mice and their littermate control mice at the age of 12–14 weeks were treated with one dose of tamoxifen (700 mg/kg b.w.) via intraperitoneal injection (i.p.). The cerebral cortex was freshly collected on dpi7 for total RNA extraction (RNeasy Mini kit, Qiagen #74104). RNAseq library was prepared by DNA SMART ChIP Seq Kit (TAKARA #101617). RNA Sequencing was performed on Illumina NextSeq 500 desktop Next Generation Sequencing (NGS) system. Sequencing reads were aligned to the mouse reference genome GENCODE Version M9. Differentially expressed genes were identified by normalized ratio of Reads Per Kilobase of transcript per million mapped reads (RPKM) between the *Tak1 CKO* and littermate control mice.

Fastp[65] was recruited to low-quality reads and adaptor trimming with a default setting[66] (http://www.usadellab.org/cms/?page=trimmomatic). Cleaned reads were mapped to the ensembl mouse

reference genome GRCm38.p6 (http://asia.ensembl.org/Mus_musculus/ Info/Index) using STAR alignment software[67]. The mapped reads were counted to genes using featureCounts (http://subread.sourceforge.net/). Differential expression analysis was performed using DESeq2 (https://bioconductor.org/packages/release/bioc/html/DESeq2.html) with a cutoff of FDR < 0.05 and abs (log2FC)>1. Volcano plot, Scatter plotting, and heatmaps were generated using R packages (ggplot2; pheatmap) implemented in R Studio.

Volcano plot representing significantly up- and down-regulated genes. *Padj*, adjusted *p* value. The thresholds are FC > 2 and *Padj* (FDR) < 0.05 for Ctrl ($n = 4$ mice) and *Tak1 CKO* ($n = 4$ mice). Up-regulated and down-regulated genes are highlighted in pink and light blue, respectively; black vertical lines highlight FC of −1.5 and 1.5, while black horizontal lines represent a *P*adj of 0.05 (Fig. 8).

GO and KEGG enrichment analysis

Functional enrichment in GO terms (Cellular Component; Biological Process; Molecular Function) of differential expression genes (FDR < 0.05 & |FC|>2) was performed using the clusterProfiler R package[68], setting a q value threshold of 0.05 for statistical significance.

GSEA analysis

The mechanisms underlying the relationship between blood vascular regression and neuron activity depression were explored with GSEA[69]. For gene set enrichment analysis (GSEA), we generated a KEGG_2019_Mouse geneset based on a database file from Enrichr online library (https://amp.pharm.mssm.edu/Enrichr/)[70]. Genes were pre-ranked through the metrics algorithm (we applied sign of log fold change * -log10(p-value [not adjusted *p*-val)]; statistical result of DESeq2. Pre-ranked (.rnk) file and custom geneset were used as input for GSEA v4.0.3 (https://www.gsea-msigdb.org/gsea/index.jsp). The number of permutations was set at 1000 and enrichment statistics were set at "weighted". For the general significance threshold, false discovery rate (FDR) q-val <0.25 and |NES| > 1.5 were considered as significant enrichment.

Statistics and reproducibility

All quantitative data were analyzed using Imaris 10.0 and GraphPad Prism 9.0. Differences between the two groups were assessed using two-tailed paired or unpaired Student's *t*-tests. Data are presented as mean ± SEM. Statistical significance was defined as follows unless otherwise specified: *, $p < 0.05$; **, $p < 0.01$; ***, $p < 0.005$.

Data availability

Source data are provided with this paper. The bulk RNA-seq data for *Tak1 CKO* and littermate control mice with cortex are publicly available from NCBI GEO (accession numbers GSE 296574): https://www.ncbi.nlm.nih.gov/geo/query/acc.cgi?acc=GSE296574. The metabolomics data generated in this study have been included in Source data.

Code availability

No custom code or mathematical algorithms were developed in this study.

References

1. Armulik, A., Genove, G. & Betsholtz, C. Pericytes: developmental, physiological, and pathological perspectives, problems, and promises. *Dev. cell* **21**, 193–215 (2011).
2. Zhang, Z. G. et al. Three-dimensional measurement of cerebral microvascular plasma perfusion, glial fibrillary acidic protein and microtubule associated protein-2 immunoreactivity after embolic stroke in rats: a double fluorescent labeled laser-scanning confocal microscopic study. *Brain Res* **844**, 55–66 (1999).
3. Bélanger, M., Allaman, I. & Magistretti, P. J. Brain energy metabolism: focus on astrocyte-neuron metabolic cooperation. *Cell Metab* **14**, 724–738 (2011).
4. Barres, B. A. The mystery and magic of glia: a perspective on their roles in health and disease. *Neuron* **60**, 430–440 (2008).
5. Chen, B. R., Kozberg, M. G., Bouchard, M. B., Shaik, M. A. & Hillman, E. M. A critical role for the vascular endothelium in functional neurovascular coupling in the brain. *J. Am. Heart Assoc.* **3**, e000787 (2014).
6. Abbott, N. J., Ronnback, L. & Hansson, E. Astrocyte-endothelial interactions at the blood-brain barrier. *Nat. Rev. Neurosci.* **7**, 41–53 (2006).
7. Iadecola, C. The Neurovascular Unit Coming of Age: A Journey through Neurovascular Coupling in Health and Disease. *Neuron* **96**, 17–42 (2017).
8. Riddle, D. R., Sonntag, W. E. & Lichtenwalner, R. J. Microvascular plasticity in aging. *Ageing Res. Rev.* **2**, 149–168 (2003).
9. Bell, M. A. & Ball, M. J. Morphometric comparison of hippocampal microvasculature in ageing and demented people: diameters and densities. *Acta Neuropathol.* **53**, 299–318 (1981).
10. Brown, W. R. & Thore, C. R. Review: cerebral microvascular pathology in ageing and neurodegeneration. *Neuropathol. Appl. Neurobiol.* **37**, 56–74 (2011).
11. Kaplan, L., Chow, B. W. & Gu, C. Neuronal regulation of the blood-brain barrier and neurovascular coupling. *Nat. Rev. Neurosci.* **21**, 416–432 (2020).
12. Chow, B. W. et al. Caveolae in CNS arterioles mediate neurovascular coupling. *Nature* **579**, 106–110 (2020).
13. Coelho-Santos, V. & Shih, A. Y. Postnatal development of cerebrovascular structure and the neurogliovascular unit. *Wiley Interdiscip. Rev. Dev. Biol.* **9**, e363 (2020).
14. Rao, S. et al. Obligatory participation of macrophages in an angiopoietin 2-mediated cell death switch. *Development* **134**, 4449–4458 (2007).
15. Korn, C. et al. Endothelial cell-derived non-canonical Wnt ligands control vascular pruning in angiogenesis. *Development* **141**, 1757–1766 (2014).
16. Franco, C. A. et al. Dynamic endothelial cell rearrangements drive developmental vessel regression. *PLoS Biol.* **13**, e1002125 (2015).
17. Hughes, S. Chang-Ling T. Roles of endothelial cell migration and apoptosis in vascular remodeling during development of the central nervous system. *Microcirculation* **7**, 317–333 (2000).
18. Chen, Q. et al. Haemodynamics-driven developmental pruning of brain vasculature in zebrafish. *PLoS Biol.* **10**, e1001374 (2012).
19. Lenard, A. et al. Endothelial cell self-fusion during vascular pruning. *PLoS Biol.* **13**, e1002126 (2015).
20. Lobov, I. B. et al. WNT7b mediates macrophage-induced programmed cell death in patterning of the vasculature. *Nature* **437**, 417–421 (2005).
21. Phng, L. K. et al. Nrarp coordinates endothelial Notch and Wnt signaling to control vessel density in angiogenesis. *Dev. Cell* **16**, 70–82 (2009).
22. Baffert, F. et al. Cellular changes in normal blood capillaries undergoing regression after inhibition of VEGF signaling. *Am. J. Physiol. Heart Circ. Physiol.* **290**, H547–H559 (2006).
23. Inai, T. et al. Inhibition of vascular endothelial growth factor (VEGF) signaling in cancer causes loss of endothelial fenestrations, regression of tumor vessels, and appearance of basement membrane ghosts. *Am. J. Pathol.* **165**, 35–52 (2004).
24. Hammes, H. P. et al. Angiopoietin-2 causes pericyte dropout in the normal retina: evidence for involvement in diabetic retinopathy. *Diabetes* **53**, 1104–1110 (2004).
25. Zhu, X., Bergles, D. E. & Nishiyama, A. NG2 cells generate both oligodendrocytes and gray matter astrocytes. *Development* **135**, 145–157 (2008).

26. Jia, J. M. et al. Control of cerebral ischemia with magnetic nanoparticles. *Nat. Methods* **14**, 160–166 (2017).
27. Hill, R. A. et al. Regional blood flow in the normal and ischemic brain is controlled by arteriolar smooth muscle cell contractility and not by capillary pericytes. *Neuron* **87**, 95–110 (2015).
28. Cammermeyer, J. A comparative study of intervascular connective tissue strands in the central nervous system. *J. Comp. Neurol.* **114**, 189–208 (1960).
29. Brown, W. R. A review of string vessels or collapsed, empty basement membrane tubes. *J. Alzheimers Dis.* **21**, 725–739 (2010).
30. Challa, V. R., Thore, C. R., Moody, D. M., Brown, W. R. & Anstrom, J. A. A three-dimensional study of brain string vessels using celloidin sections stained with anti-collagen antibodies. *J. Neurol. Sci.* **203-204**, 165–167 (2002).
31. Cuttler, A. S. et al. Characterization of Pdgfrb-Cre transgenic mice reveals reduction of ROSA26 reporter activity in remodeling arteries. *Genesis* **49**, 673–680 (2011).
32. Sorensen, I., Adams, R. H. & Gossler, A. DLL1-mediated Notch activation regulates endothelial identity in mouse fetal arteries. *Blood* **113**, 5680–5688 (2009).
33. Zong, H., Espinosa, J. S., Su, H. H., Muzumdar, M. D. & Luo, L. Mosaic analysis with double markers in mice. *Cell* **121**, 479–492 (2005).
34. Tang, S. H., Silva, F. J., Tsark, W. M. & Mann, J. R. A. Cre/loxP-deleter transgenic line in mouse strain 129S1/SvImJ. *Genesis* **32**, 199–202 (2002).
35. Hippenmeyer, S., Johnson, R. L. & Luo, L. Mosaic analysis with double markers reveals cell-type-specific paternal growth dominance. *Cell Rep.* **3**, 960–967 (2013).
36. Alarcon-Martinez, L. et al. Interpericyte tunnelling nanotubes regulate neurovascular coupling. *Nature* **585**, 91–95 (2020).
37. Iadecola, C. & Nedergaard, M. Glial regulation of the cerebral microvasculature. *Nat. Neurosci.* **10**, 1369–1376 (2007).
38. Zhuo, L. et al. Live astrocytes visualized by green fluorescent protein in transgenic mice. *Dev. Biol.* **187**, 36–42 (1997).
39. Gong, S. et al. A gene expression atlas of the central nervous system based on bacterial artificial chromosomes. *Nature* **425**, 917–925 (2003).
40. Ridder, D. A. et al. Brain endothelial TAK1 and NEMO safeguard the neurovascular unit. *J. Exp. Med* **212**, 1529–1549 (2015).
41. Körbelin, J. et al. A brain microvasculature endothelial cell-specific viral vector with the potential to treat neurovascular and neurological diseases. *EMBO Mol. Med.* **8**, 609–625 (2016).
42. Ridder, D. A. et al. TAK1 in brain endothelial cells mediates fever and lethargy. *J. Exp. Med* **208**, 2615–2623 (2011).
43. Xiong, N. et al. Using arterial-venous analysis to characterize cancer metabolic consumption in patients. *Nat. Commun.* **11**, 3169 (2020).
44. Nikolakopoulou, A. M. et al. Pericyte loss leads to circulatory failure and pleiotrophin depletion causing neuron loss. *Nat. Neurosci.* **22**, 1089–1098 (2019).
45. Kolb, B. & Whishaw, I. Q. Brain plasticity and behavior. *Annu. Rev. Psychol.* **49**, 43–64 (1998).
46. Reeson P., Choi K., Brown C. E. VEGF signaling regulates the fate of obstructed capillaries in mouse cortex. *Elife* **7**, e33670 (2018).
47. Rivard, A. et al. Age-dependent defect in vascular endothelial growth factor expression is associated with reduced hypoxia-inducible factor 1 activity. *J. Biol. Chem.* **275**, 29643–29647 (2000).
48. Frenkel-Denkberg, G., Gershon, D. & Levy, A. P. The function of hypoxia-inducible factor 1 (HIF-1) is impaired in senescent mice. *FEBS Lett.* **462**, 341–344 (1999).
49. Ren, J. et al. Somatic variants of MAP3K3 are sufficient to cause cerebral and spinal cord cavernous malformations. *Brain* **146**, 3634–3647 (2023).
50. Helmlinger, G., Yuan, F., Dellian, M. & Jain, R. K. Interstitial pH and pO_2 gradients in solid tumors in vivo: high-resolution measurements reveal a lack of correlation. *Nat. Med* **3**, 177–182 (1997).
51. Baish, J. W. et al. Scaling rules for diffusive drug delivery in tumor and normal tissues. *Proc. Natl. Acad. Sci. USA* **108**, 1799–1803 (2011).
52. Nicholson, C. Diffusion and related transport mechanisms in brain tissue. *Rep. Prog. Phys.* **64**, 815–884 (2001).
53. Hatazawa, J., Shimosegawa, E., Satoh, T., Toyoshima, H. & Okudera, T. Subcortical hypoperfusion associated with asymptomatic white matter lesions on magnetic resonance imaging. *Stroke* **28**, 1944–1947 (1997).
54. Lacoste, B. et al. Sensory-related neural activity regulates the structure of vascular networks in the cerebral cortex. *Neuron* **83**, 1117–1130 (2014).
55. Hall, C. N. et al. Capillary pericytes regulate cerebral blood flow in health and disease. *Nature* **508**, 55–60 (2014).
56. Zlokovic, B. V. Neurovascular pathways to neurodegeneration in Alzheimer's disease and other disorders. *Nat. Rev. Neurosci.* **12**, 723–738 (2011).
57. Magistretti, P. J. & Allaman, I. A cellular perspective on brain energy metabolism and functional imaging. *Neuron* **86**, 883–901 (2015).
58. Ge, W. P., Miyawaki, A., Gage, F. H., Jan, Y. N. & Jan, L. Y. Local generation of glia is a major astrocyte source in postnatal cortex. *Nature* **484**, 376–380 (2012).
59. Barson, D. et al. Simultaneous mesoscopic and two-photon imaging of neuronal activity in cortical circuits. *Nat. Methods* **17**, 107–113 (2020).
60. Xu P. et al. Pattern decorrelation in the mouse medial prefrontal cortex enables social preference and requires MeCP2. *Nat. Commun.* **13**, 3899 (2022).
61. Yue Y. et al. Motor training improves coordination and anxiety in symptomatic Mecp2-null mice despite impaired functional connectivity within the motor circuit. *Sci. Adv.* **7**, 7467 (2021).
62. Jing, D. et al. Tissue clearing of both hard and soft tissue organs with the PEGASOS method. *Cell Res* **28**, 803–818 (2018).
63. Yu J. et al. Metabolic abnormalities in patients with chronic disorders of consciousness. *Aging Dis* **12**, 386–403 (2021).
64. Chong, J. et al. MetaboAnalyst 4.0: towards more transparent and integrative metabolomics analysis. *Nucleic Acids Res.* **46**, W486–W494 (2018).
65. Chen, S., Zhou, Y., Chen, Y. & Gu, J. fastp: an ultra-fast all-in-one FASTQ preprocessor. *Bioinformatics* **34**, i884–i890 (2018).
66. Bolger, A. M., Lohse, M. & Usadel, B. Trimmomatic: a flexible trimmer for Illumina sequence data. *Bioinformatics* **30**, 2114–2120 (2014).
67. Dobin, A. et al. STAR: ultrafast universal RNA-seq aligner. *Bioinformatics* **29**, 15–21 (2013).
68. Yu, G., Wang, L. G., Han, Y. & He, Q. Y. clusterProfiler: an R package for comparing biological themes among gene clusters. *OMICS* **16**, 284–287 (2012).
69. Reimand, J. et al. Pathway enrichment analysis and visualization of omics data using g:Profiler, GSEA, Cytoscape and EnrichmentMap. *Nat. Protoc.* **14**, 482–517 (2019).
70. Chen, E. Y. et al. Enrichr: interactive and collaborative HTML5 gene list enrichment analysis tool. *BMC Bioinforma.* **14**, 128 (2013).

Acknowledgements

The project was initiated in the Jan lab at UCSF. We thank Lily Jan and Yuh-Nung Jan's generous support. We thank Liqun Luo's lab for providing MADM-7 mice and Rolf A Brekken for VEGF-antibodies. Drs. Yuanquan Song (UPenn), Zhaozhu Hu (JHU), Ji Hu (ShanghaiTech), Yang Xiang (U. Mass), Hao Wang (Zhejiang U.) and Ruikang Wang (U. Washington) for critical input, colleagues at Children's Research Institute, Departments of Neuroscience, Neurology and Neurotherapeutics, Pediatrics from UT Southwestern, and colleagues from the Jan lab for discussion. Dr. Bridget Samuels, for critical reading. We acknowledge the assistance of the CIBR Imaging core. This work was supported by

grants from the STI2030-Major Projects (2022ZD0204700), CAMS Innovation Fund for Medical Sciences (CIFMS, 2024-I2M-ZD-012), the National Natural Science Foundation of China (32170964), and funds from CIBR to W.G., grants from National Natural Science Foundation of China to J.M.J, (32170961), National Natural Science Foundation of China (No. 31800864), Westlake University start-up funds to J-M. J. and German Research Foundation, DFG (No. 335447717) to J.K. German Research Foundation (DFG, No 523830300) to M.T. and J.K. We also thank UT Southwestern Live Cell Imaging Facility, a Shared Resource of the Harold C. Simmons Cancer Center, supported in part by an NCI Cancer Center Support Grant, P30 CA142543K. This work is also supported by the American Heart Association AWRP Summer 2016 Innovative Research Grant (17IRG33410377) to W-P.G.; National Natural Science Foundation of China (No. 81370031) to Z.Z.; National Key Research and Development Program of China (2016YFE0125400) to F.H.; National Natural Science Foundations of China (No. 81473202) to Y.L.; National Natural Science Foundation of China (No.31600839) and Shenzhen Science and Technology Research Program (JCYJ20170818163320865) to B.P.; NIH: R01 AG020670 and RF1AG054111 to H.Z.; R01 NS088555 to A.M.S., and European Research Council No.725780 to S.H.; W-P.G. was a recipient of Bugher-American Heart Association Dan Adams Thinking Outside the Box Award.

Author contributions

W-P.G. and X.G. conceived the project. X.G., W-P.G., X-J. C. designed experiments. X.G. and X-J. C. performed all in vivo imaging experiments in animals and analyzed data. X.G., W-P.G., X-J. C., M. Y., B.C., J-L.L., D.Y., L.Z., Z.B., N.L., Y(Yating). Y., F.C., J-M.J., B.S., Y(Yuanlei). Y., S.Z., Y-C. S., K.S., N.E.P., Y.H., X(Xinwei). G., T. L., J. L., K.P., Z.Z., K.S., D.B.B., F(Fen) H., S-B.Y. performed the other experiments and analysis. W-P.G. R.H.A., V.L., L-J W, B.P., H(Hu). Z., B.O.Z., F(Feng). H., S.H., A.M.S., M.M., X.W., Q.L., Y-M. L., J. K., M. T., H. L., J. J-M., R.M.B., Q.G., G.C., W.S. and H(Hui). Z. provided assistance in experimental design and data analysis. W-P.G., X.G., X-J. C. and M. Y. wrote the manuscript. All authors reviewed and edited the manuscript.

Competing interests

The authors declare no competing interests.

Additional information

Supplementary information The online version contains supplementary material available at https://doi.org/10.1038/s41467-025-60308-0.

Correspondence and requests for materials should be addressed to Woo-ping Ge.

Peer review information *Nature Communications* thanks Eric Dammer, Angeliki Nikolakopoulou, and the other anonymous reviewer(s) for their contribution to the peer review of this work. A peer review file is available.

[1]Children's Research Institute, University of Texas Southwestern Medical Center, Dallas, TX 75390, USA. [2]Chinese Institute for Brain Research, Beijing, Beijing 102206, China. [3]Beijing Institute for Brain Research, Chinese Academy of Medical Sciences & Peking Union Medical College, Beijing 102206, China. [4]Academy for Advanced Interdisciplinary Studies (AAIS), Peking University, Beijing 100871, China. [5]School of Basic Medical Sciences, Capital Medical University, Beijing 100069, China. [6]Changping Laboratory, Beijing 102206, China. [7]Institute of Pharmacology and Toxicology, College of Pharmaceutical Sciences, Zhejiang University, Hangzhou 310058, China. [8]School of Basic Medical Sciences, Jiangxi Medical College, Nanchang University, Nanchang 330031, China. [9]State Key Laboratory of Oral Diseases, National Center for Stomatology, National Clinical Research Center for Oral Diseases, West China Hospital of Stomatology, Sichuan University, Chengdu 610041, China. [10]College of Life Sciences, Nankai University, Tianjin 300071, China. [11]GW Institute for Neuroscience, the George Washington University, Washington, DC 20037, USA. [12]Institute of Basic Medical Sciences, Westlake Institute for Advanced Study, Westlake Laboratory of Life Sciences and Biomedicine, School of Life Sciences, Westlake University, Hangzhou 310024, China. [13]Department of Medical College, Fujian Health College, Fuzhou 350101, China. [14]Guangdong Institute of Intelligence Science and Technology, Guangdong 519031, China. [15]Department of Neurology, Beijing Tiantan Hospital, Capital Medical University; Chinese Institutes for Medical Research, Beijing 100069, China. [16]Huffington Center on Aging, Baylor College of Medicine, Houston, TX 77030, USA. [17]Shenzhen Institutes of Advanced Technology, Chinese Academy of Sciences, Shenzhen 518055, China. [18]Department of Neurology and Neurotherapeutics, University of Texas Southwestern Medical Center, Dallas TX75390, USA. [19]Department of Laboratory Medicine, Changzheng Hospital, Naval Medical University, Shanghai 200003, China. [20]Department of Neurology, Mayo Clinic, Rochester, MN 55905, USA. [21]Departments of Physiology, Biochemistry and Biophysics, University of California at San Francisco, San Francisco, CA 94158, USA. [22]Institute of Biomedical Sciences, Academia Sinica, Taipei 115, Taiwan. [23]Department of Tissue Morphogenesis, Max-Planck-Institute for Molecular Biomedicine, and Faculty of Medicine, University of Münster, D-, 48149 Münster, Germany. [24]Center for Molecular Medicine, MaineHealth Institute for Research, Scarborough ME04074, USA. [25]Institute of Science and Technology Austria, Am Campus 1, 3400 Klosterneuburg, Austria. [26]Department of Biology, Stanford University, Stanford CA94305, USA. [27]Neurology, University of Kentucky, Lexington, KY 40536, USA. [28]Department of Neurosurgery, Huashan Hospital, Institute for Translational Brain Research, State Key Laboratory of Medical Neurobiology, MOE Frontiers Center for Brain Science, MOE Innovative Center for New Drug Development of Immune Inflammatory Diseases, Fudan University, Shanghai 200040, China. [29]Department of Pathology, University of California at San Francisco, San Francisco, CA 94143, USA. [30]School of Biomedical Engineering, Capital Medical University, Beijing 100069, China. [31]State Key Laboratory of Brain and Cognitive Science, Institute of Biophysics, Chinese Academy of Sciences, Beijing 100101, China. [32]State Key Laboratory of Cognitive Neuroscience and Learning, New Cornerstone Science Laboratory, Beijing Normal University, Beijing 100875, China. [33]Department of Neurology, Tianjin Neurological Institute,

Tianjin Medical University General Hospital, Tianjin 300052, China. [34]Department of Oncology, Hematology and Bone Marrow Transplantation, University Medical Center Hamburg-Eppendorf, 20246 Hamburg, Germany. [35]Department of Hematology and Clinical Oncology, University Medical Center and Medical Faculty Augsburg University, Augsburg 86156, Germany. [36]Department of Pharmacology and Physiology, School of Medicine and Health Sciences, the George Washington University, Washington, DC 20037, USA. [37]Key Laboratory of Multi-Cell Systems, Shanghai Institute of Biochemistry and Cell Biology, Chinese Academy of Sciences; University of Chinese Academy of Sciences, Shanghai 200031, China. [38]National Institute of Biological Sciences, Beijing (NIBS), 102206 Beijing, China. [39]Tsinghua Institute of Multidisciplinary Biomedical Research, Tsinghua University, 100084 Beijing, China. [40]Key Laboratory of Modern Toxicology of Ministry of Education; School of Basic Medical Sciences, Nanjing Medical University, Nanjing 211166, China. [41]Medical Basic Research Innovation Center for Cardiovascular and Cerebrovascular Diseases, Ministry of Education, China; International Joint Laboratory for Drug Target of Critical Illnesses, School of Pharmacy, Nanjing Medical University, Nanjing 211166, China. [42]Department of Internal Medicine, University of Texas Southwestern Medical Center, Dallas, TX 75390, USA. [43]Present address: Takeda Pharmaceuticals, Cambridge, MA 02142, USA. [44]These authors contributed equally: Xiaofei Gao, Xing-jun Chen. ✉e-mail: woopingge@cibr.ac.cn